Sensor and control development for a laser tracking system

Linssen, S.

Award date:
1998

7610

Eindhoven University of Technology
Department of Electrical Engineering
Measurement and Control Group

Sensor and control development for a laser tracking system

by
S. Linssen

Master of Science Thesis
carried out from November 1997 to August 1998
commissioned by prof. dr. ir. P. van den Bosch
under supervision of dr. ir. A. Damen, dr. ir. R. Gorter and dr. ir. A. Veltman
date: August 26, 1998

ABSTRACT

A laser tracking system is used to track the tool center point (TCP) of a robot. A laser beam is pointed to the center of a mirror and deflected to a retroreflector attached to the TCP. The beam coming from the retroreflector is guided to a position sensing detector, which output is used to adjust the tilting of the mirror to keep the beam in the center of the retroreflector. The mirror is beared on an air cushion and can be tilted by the forces of three actuators. Therefore, there is no mechanical friction and in particular no slipstick.

For calculation of the retroreflectors position the tilting of the mirror is determined in two directions. This is done by an inductive sensor. However, the angles are only reliable if the air gap of the mirror is constant. The air gap is measured by a capacitive sensor. Two controllers are needed: an air gap controller and an angle controller.

The study described in this report concerns the improvement of the sensors and the design of the air gap and angle controllers.

In particular the electronics for the angle and air gap sensors have been improved. Both are based on a LVDT-signal conditioner (AD698). In this way drift of the oscillator amplitude doesn't influence the measurement. To minimize the influence from temperature variations of the primary coil used for the angle measurement, the coil was optimized within the mechanical constraints and a circuit was developed to approximate the voltage over the inductance of the coil, needed by the LVDT.

The dependence of the air gap transfer function on the air gap was determined with a frequency response measurement. The measurements revealed several resonance frequencies, not predicted by the simple model available, most of them depending on the air gap. An air gap controller was designed, implemented and tested on the real system using a DSP system. The controlled bandwidth was reached by choosing an adequate air gap, resulting in a shift of the resonance frequencies to higher frequencies.

After design and implementation of the angle controllers the tracking system was tested and found able to perform the aimed task.

1. INTRODUCTION.

The Measurement and Control Group of the Department of Electrical Engineering at Eindhoven University of Technology is doing research on modeling, identification and control of processes. One of these processes is a laser tracking system, which is shown in Figure 1.1.

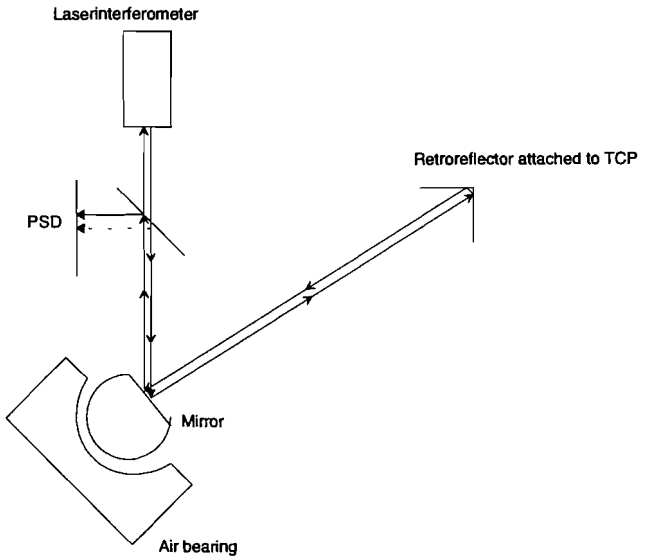

Figure 1.1 The laser tracking system.

The crucial part is a mirror rotating in a spherical air bearing. The laser beam is pointed at the rotatable mirror's center and then deflected to a retroreflecter attached to the tools center point (TCP) of a robot. The retroreflector returns the laser beam parallel to the incoming beam, independent of the angle of incidence. The reflected laser beam is split into two by a half-way mirror. One part is deflected towards a position sensing detector (from now on abbreviated as PSD) that measures the position of the incoming laser beam in two coordinates. These coordinates represent the deviation of the reflected laser beam from the retroreflector's center. On the basis of these two coordinates the tracking controller adjusts the mirror so that the laser beam is pointed towards the center of the TCP. (Remark: In the drawing the incoming and returned laser beam are drawn parallel to make the path understandable. In the real system they should fall together if the laser beam hits the retroreflector in the center (dotted arrow).) The nondeflected beam is used by a laser-interferometer or a laser-distancemeter to calculate the distance the laser beam has traveled.

The tilting of the mirror can be described by two angles. These angles represent also the deflection of the laser beam. The measurement of these two angles combined with the distance measurement enables a calculation of the position of the TCP.

The tracking system should meet two goals:
1. It should measure the TCP with a (theoretically) zero steady-state error.
2. It should follow the retroreflector even when the robot is moving at high speed.

Besides the tracking mode mentioned above one also needs a scanning mode. If the laser beam has lost the TCP due to some reason the system should be able to find the TCP. This

can be done by moving the laser beam in a pattern across the room. If the beam hits the retroreflector the PSD measures an incoming beam and the system can be switched to the tracking mode.

One goal of my master thesis was to implement the tracking mode. This means that an air gap controller for the air bearing and a PSD-error controller have to be developed. The second goal was the improvement of the sensors used. An overview of the total system is shown below in block form.

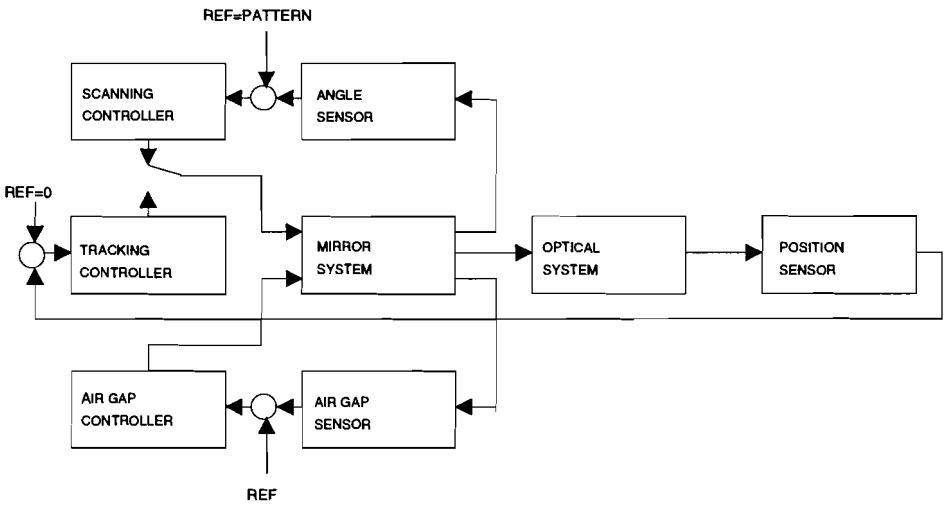

Figure 1.2 Block scheme of the tracking and scanning mode.

In the next chapter the mechanical part of the mirror system will be described. Chapter 3 discusses the improvement of the sensors. Chapter 4 is devoted to the development and implementation of the controllers for the tracking mode. Chapter 5 includes the conclusions and recommendations.

2. DESCRIPTION OF THE MIRROR SYSTEM.

In this chapter the mirror system will be described together with the models developed.

2.1 MECHANICAL DESCRIPTION OF THE MIRROR.

The mirror consists of a steel semi sphere rotating on an air bearing. As can be seen in Figure 2.1 three electromagnetic actuators are connected via strings (twaron) to a plastic ring (this ring has a U-profile, in the U the primary coil is seated). In the center of the plastic ring the mirror is attached. By pulling and revealing the strings the mirror is rotated. Besides this rotation the mirror's height can also be influenced by pulling or revealing all the three strings at the same time with equal force.

These movements are described with three coordinates: h (height), α and β (tilting).

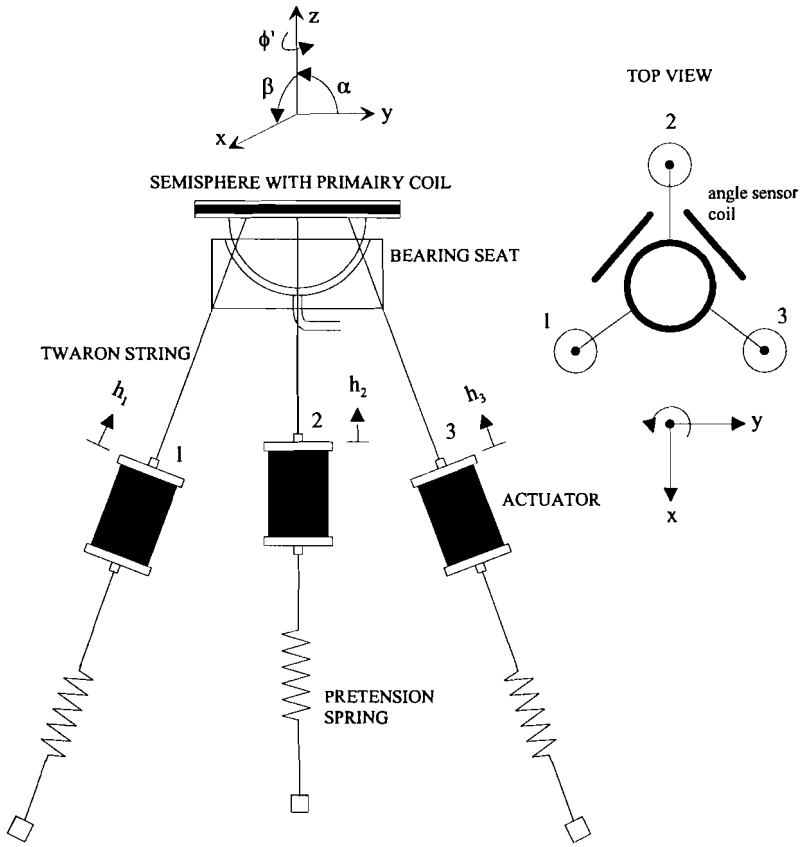

Figure 2.1 Structural overview of mechanics mirror system.

Because the moveable parts of this system float on (the mirror) or in (moveable part of actuators) air there is no mechanical friction and in particular no slipstick.

2.2 MODELING OF THE MIRROR SYSTEM

The mirror can be modeled by Euler-Lagrange equations [Noten]:

$$\underline{v} = \dot{\underline{p}}$$

$$M(\underline{p})\,\dot{\underline{v}} = \underline{Q}(\underline{v},\underline{p},t) + \underline{F}(t) + \underline{G}^T(\underline{p})\underline{\lambda} \qquad (2.1)$$

$$g(\underline{p}) = \underline{0}$$

$\underline{p}$ is the vector of generalized coordinates, here $\underline{p}=(\alpha,\beta,\phi',h_1,h_2,h_3)^T$. α and β describe the tilting of the mirror about the x-axis and y-axis ,respectively. ϕ' is the rotation of the mirror about the axis perpendicular to axis α and β. h_1,h_2 and h_3 are the heights of the moveable cores of the three actuators in relation to their rest position. M is the inertia matrix of the complete system. $\underline{Q}$ represents the Coriolis and centrifugal forces and $\underline{F}$ are the forces acting on the system. The Lagrange multiplier $\underline{\lambda}$ represents the magnitudes of the constraint forces. The direction of the constraint forces is determined by the matrix G^T, where G is defined as the Jacobian of $\underline{g}(\underline{p})$. $\underline{g}(\underline{p})$ represents the geometrical constraints on the system. In Appendix A the values for M, Q, F, G and $\underline{g}(\underline{p})$ are shown.

This set of equations form a so called index-3 Differential Algebraic Equation (DAE). Before these equations can be used for building a linear controller one needs to linearize these equations and transform the linearized equations into a set of Ordinary Differential Equations (ODE). When linearizing the equations one needs to choose a working point. If the rest position $\alpha=\beta=\phi'=h_1=h_2=h_3=0$ is chosen the following result [Noten] is obtained:

$$\alpha = \frac{r\sqrt{3}A(U_2 - U_3)}{as^3 + bs^2 + cs + d}$$

$$\beta = \frac{r(-2U_1 + U_2 + U_3)A}{as^3 + bs^2 + cs + d} \qquad (2.2)$$

Where U_1,U_2 and U_3 are the Laplace transforms of the input voltages to the actuators. For the meaning of the other parameters see Appendix B.

To simplify the functions further the matrices T and $\tilde{T}$ are introduced:

$$T = \begin{pmatrix} 0 & \sqrt{3} & -\sqrt{3} \\ -2 & 1 & 1 \end{pmatrix}$$

$$\tilde{T} = \begin{pmatrix} 0 & -\frac{1}{3} \\ \frac{1}{6}\sqrt{3} & \frac{1}{6} \\ -\frac{1}{6}\sqrt{3} & \frac{1}{6} \end{pmatrix} \qquad (2.3)$$

such that with

$$\begin{pmatrix} U_\alpha \\ U_\beta \end{pmatrix} = T \begin{pmatrix} U_1 \\ U_2 \\ U_3 \end{pmatrix}$$
$$\begin{pmatrix} U_1 \\ U_2 \\ U_3 \end{pmatrix} = \tilde{T} \begin{pmatrix} U_\alpha \\ U_\beta \end{pmatrix} \qquad (2.4)$$

the equations can be written as:

$$\alpha = \frac{r\sqrt{3}AU_\alpha}{as^3 + bs^2 + cs + d}$$
$$\beta = \frac{rU_\beta A}{as^3 + bs^2 + cs + d} \qquad (2.5)$$

These transfer functions are the ones needed because the actual system has as control inputs for the actuators U_α and U_β. The transformation to U_1, U_2 and U_3 is done in hardware.

In the real system the transformation from the inputs U_h (the voltage controlling the air gap, is the average of U_1,U_2 and U_3), U_α and U_β to U_1, U_2 and U_3, respectively, is done via:

$$\begin{pmatrix} U_1 \\ U_2 \\ U_3 \end{pmatrix} = \begin{pmatrix} \frac{1}{3} & 0 & -\frac{2}{3} \\ \frac{1}{3} & \frac{1}{3}\sqrt{3} & \frac{1}{3} \\ \frac{1}{3} & -\frac{1}{3}\sqrt{3} & \frac{1}{3} \end{pmatrix} \begin{pmatrix} U_h \\ U_\alpha \\ U_\beta \end{pmatrix} \qquad (2.6)$$

Because (**2.6**) is used the right parts of the transfer functions (**2.5**) have to be multiplied with a factor two to obtain the transfer functions.

Both transfer function are of third order. Every rotation of the mirror is of order 2. The three actuators would contribute a third order system to each rotation. If and only if:
1. the control of the air gap is ideal
2. the actuators and pretension strings are identical
3. the stiff spring effect from actuator to mirror is neglected

one actuator position is enough to compute the two others. So the third order is due to the electrical time constant of one actuator. The pole and bode plots are shown below in Figure 2.2.

The model used above is based on the fact that the air gap stays at a constant value [Noten] by very stiff control. It is supposed that the translation dynamics of the air gap are independent of the rotation dynamics. Therefore the control of the air gap can be superimposed on the angle control.

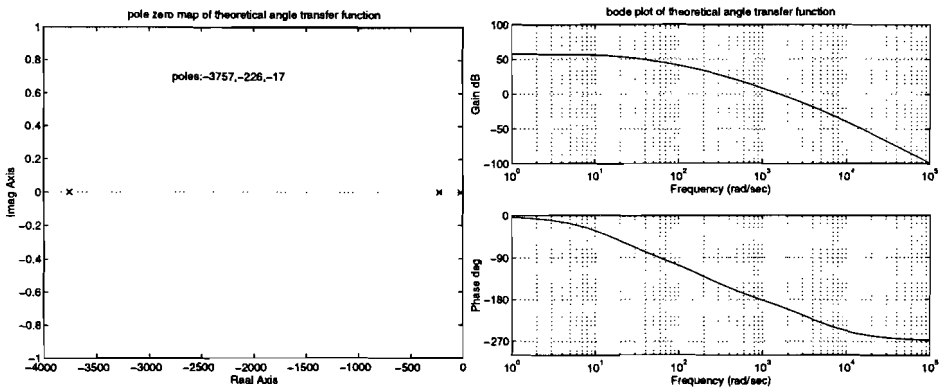

Figure 2.2 Pole zero map and bode plot of theoretical angle transfer function.

The dynamical model and its simplified version used by [Looymans] to obtain the air gap transfer function are shown in Figure 2.3.

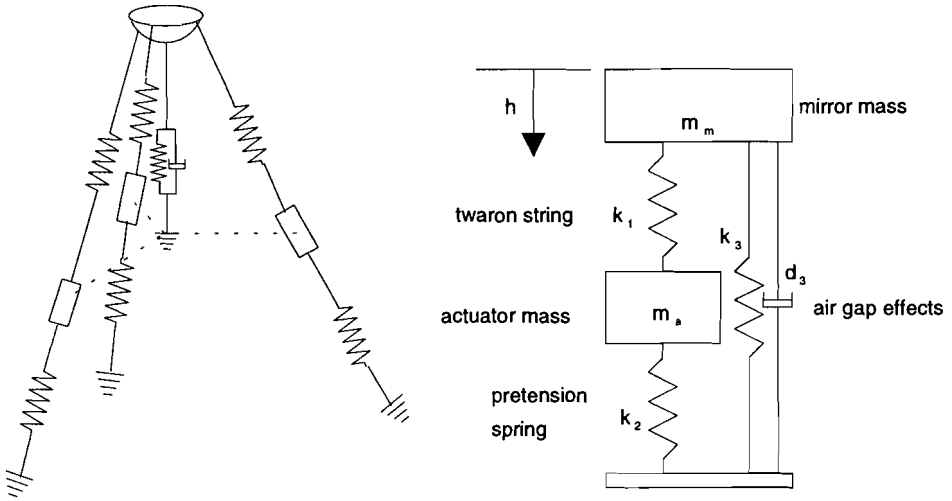

Figure 2.3 Modeling mirror system for air gap transfer function.

The pretension and twaron strings are modeled by springs. The air gap is represented as a combination of a spring and damper. Because the controlled system should be very broadbanded, the dynamics of the twaron strings are not neglected here.

This model results in the following transfer function:

$$h = \frac{a_0}{b_5 s^5 + b_4 s^4 + b_3 s^3 + b_2 s^2 + b_1 s^1 + b_0} U_h \qquad (2.7)$$

h represents the displacement of the semi sphere and U_h the voltage on each actuator (h and U_h are the Laplace transforms of h(t) and $U_h(t)$; for values of a_0, b_5, b_4, b_3, b_2, b_1, b_0 see Appendix B).

The pole plot shown in Figure 2.4 shows two resonance frequencies.

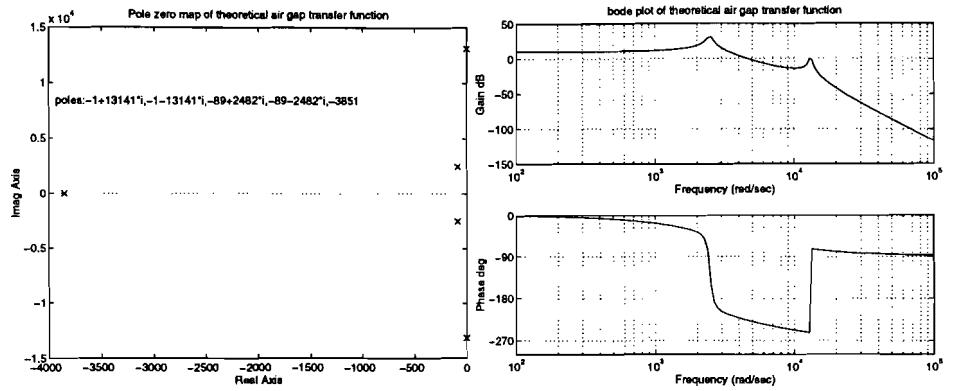

Figure 2.4 Pole zero map and bode plot of theoretical air gap transfer function.

The exact positions of the poles depend on the air friction. The poles will move towards the left if the air friction is taken greater (more damping). The pole-pair at -5±13918i (no air friction d_3=0) is caused by the mass of the semi sphere m_m in combination with spring k_1, which models the twaron strings, and k_3, which models the air stiffness. The other pole-pair at -158±4138i is caused by the mass of the actuator m_a and k_2, modeling the pretension strings. The 5th pole, at -3703, is introduced by the transfer from the force on the actuators to the voltage applied to them and determined by the impedance parameters of the actuator coil. This last pole can also be seen in the angle transfer function.

In chapter four we will take a closer look at the height transfer function because several resonance frequencies aren't modeled by it.

The need for an angle control is obvious. But why is control of the air gap necessary? This question will be answered in the next section.

2.3 WHY MODEL AND CONTROL THE AIR GAP ?

The air gap of the system will influence the accuracy of the system in two ways:

1. The deflection of the laser beam changes when the air gap height changes, because the primary laser beam doesn't hit the center of the mirror. The calculation of the TCP's position is done with the angles α and β, received from the angle sensors, and the length the laser beam has traveled, determined by the laserinterferometer. Only when the laser beam hits the center of the mirror the angles α and β represent the actual deflection of the beam.

2. The measurement of the angles of the mirror will be influenced by variation of the air gap, because:
2.1 The measurement has a certain resolution. The consequence is that the air gap will always fluctuate around a reference value with a peak-to-peak variation (expressed in meters) equal to the resolution multiplied with the sensitivity (if the controller is able to hold the reference value). This 'resolution-'variation will induce a current in the secondary coils of the angle sensor.
2.2 If the mirror height is stable (the forgoing effect doesn't play any role) but not in its zero position (the controller isn't able to hold the reference value) the flux distribution isn't the same as with the calibration of the angle sensors which is done with the air gap equal to its reference position.

Because of the foregoing reasons the air gap determines the accuracy of the whole system to a large extend. The air gap sensor's resolution and sensitivity are of crucial importance. However, the sensor for the air gap was implemented in a so called 'slave-mode'. Therefore the next chapter will start with the discussion of the angle sensor which is the (electronic) master.

3. THE SENSORS

If the designed controller can be implemented practically (e.g. available calculation power, limitations of software to implement controller etc.) the performance of the controller is limited on one side by the electro-mechanical system (including actuators) and on the other side by the bandwidth and resolution of the sensors. As mentioned in the introduction it was necessary to improve the existing angle and air gap sensors. To explain why the changes were necessary and the description of the new sensors will be the goal of this chapter.

3.1 THE ANGLE SENSORS.

In this section the disadvantages of the old sensor will be discussed first, followed by a description of the new sensor.

3.1.1 FUNCTIONAL DESCRIPTION.

3.1.1.1 Relation between input and output of coil system.

To measure the angle of the mirror, an inductive measurement system is used. The measurement system exists of two sets of inductively coupled coils, see Figure 3.1.

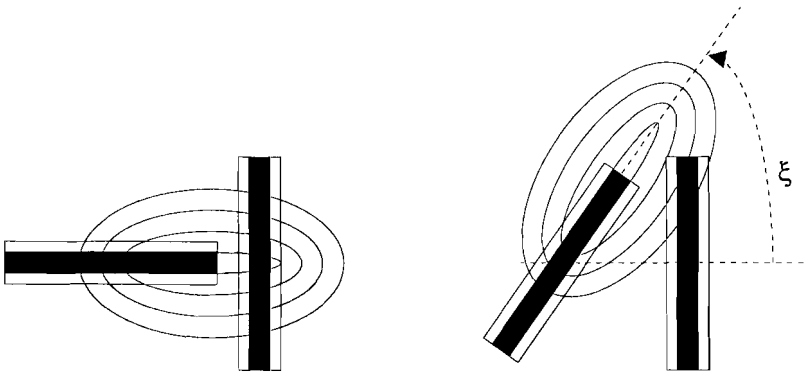

Figure 3.1 Flux lines passing through secondary coils; in equilibrium (left) tilted (right).

The primary coil (sited on the semi sphere) is energized by an external sine wave reference source. When the primary coil is in the zero position every flux line going into the secondary coil comes out of the secondary coil (left picture) so no net voltage is generated at the output of the secondary coil. If the primary coil is tilted, a part of the flux lines passes the secondary coil only ones (right picture). Therefore a net voltage is generated at the output of the secondary coil.

In [Goossens] it is derived that under the following assumptions:
1. The primary coil is positioned exactly in the middle of the secondary coils.
2. All coils are assumed to be very flat.
3. The mirror can only rotate (air gap variations will induce a current in the secondary coils).
4. The distortion of the magnetic field by the metal of the semi sphere is neglected.

The following non-linear expression between the current through the primary and secondary coil holds (for derivation see [Goossens]):

$$\frac{I_s}{I_p} = \frac{\mu_0 \mu_r N_s N_p}{4\pi L} \int_S \left(\int_l \frac{d\underline{l}(\xi) \times \underline{r}(\xi)}{\|r(\xi)\|^3} \right) \cdot \underline{n}_s dS \qquad (3.1)$$

where N_s and N_p are the number of windings of the secondary and primary coil ,respectively. L is the inductance of the secondary coil and ξ the angle the primary coil makes.

It isn't possible to solve this formula analytically for $\xi \neq 0$. [Goossens] suggested to evaluate this formula numerically. To prevent a measurement of the relation between the output of the secondary coil and the angle of the primary coil (With the accuracy wanted this is a difficult measurement!) one might consider to follow up Goossens advice. However, there are two reasons why (**3.1**) can't be used in practice:

1. With the exception of constraint 1, the assumptions made to derive this formula can't be fulfilled in the practical mirror system.

2. The parasitic capacitance between the windings in a coil, the parasitic capacitance between the coils and the end-capacitance (consisting of wires and opamps) aren't considered in deriving (**3.1**). But even if they had been considered yet another effect would prevent using above formula. Because of the parasitic capacitance's the phase between the voltages over the primary and secondary coils will depend on ξ [Zorge]. The LVDT-ic, discussed in the following section, will have a linear relationship between input (ac-voltage coming from coil) and output (dc-voltage proportional to amplitude of ac-voltage) only when the phase would have a constant value (for the time being not considering the small non-linearity always present). However, this is not the case and the sensor will have a nonlinear relationship. Therefore, one needs to measure the relationship between the angle and the output of the sensor. This measurement will be part of a calibration of the total system.

The signals coming from the secondary coils are transformed into a DC-value representing a certain angle in a coordinate system with it's x-y axis perpendicular to a plane through the secondary coils. The angles needed are however the α and β angles shown in Figure 2.1. In the following section the relationship between the different angles will be worked out.

3.1.1.2 Coordinate transformation.

The secondary coils (with perpendicular axes X_c and Y_c) are positioned at an angle of $\frac{1}{4}\pi$ rad of the real horizontal and vertical axis, as could already be seen in Figure 2.1. This is done because in this way the laserbeam can be deflected over the greatest possible range, without having to place the laser in an awkward position. The angles measured by the coils in this coordinate frame are denoted ξ_c and χ_c. See Figure 3.2. However the derived transfer functions of the previous chapter were derived for the angles α and β in the X_G,Y_G coordinate system (shown in Figure 2.1). Therefore a transformation is needed.

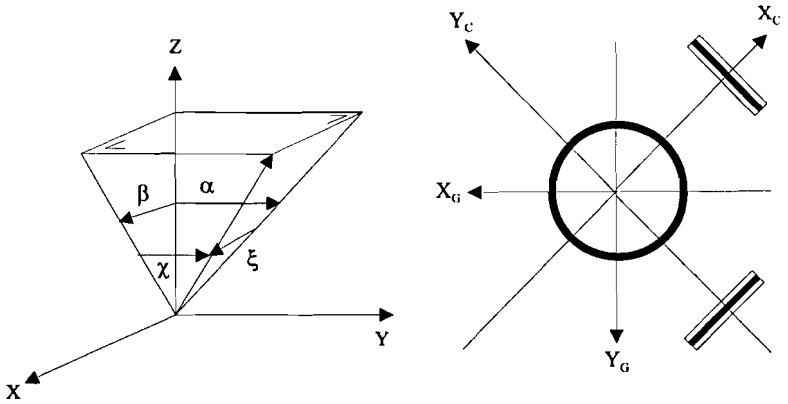

Figure 3.2 Relation between angles and coordinate systems.

The relationships between ξ_i, χ_i and α_i, β_i are non-linear:

$$\sin(\alpha_i) = \frac{\sin(\xi_i)}{\cos(\chi_i)} \qquad \sin(\beta_i) = \frac{\sin(\chi_i)}{\cos(\xi_i)} \qquad i = C(oil), G(eneral) \qquad (3.2)$$

The unit vector shown in Figure 3.2 can be written as:

$$\begin{pmatrix} x_i \\ y_i \\ z_i \end{pmatrix} = \begin{pmatrix} \sin\xi_i \\ \sin\chi_i \\ z_i \end{pmatrix} \qquad (3.3)$$

As the general coordinate frame is obtained after a -135 degrees turn about the z-axis, see Figure 3.2 (right), z_i isn't evaluated in ξ and χ.

A coordinate transformation between the two frames can be written as:

$$\begin{pmatrix} x_G \\ y_G \\ z_G \end{pmatrix} = \begin{pmatrix} -\frac{1}{2}\sqrt{2} & \frac{1}{2}\sqrt{2} & 0 \\ -\frac{1}{2}\sqrt{2} & -\frac{1}{2}\sqrt{2} & 0 \\ 0 & 0 & 1 \end{pmatrix} \begin{pmatrix} x_C \\ y_C \\ z_C \end{pmatrix} \qquad (3.4)$$

Combining (3.2) and (3.3) results in:

$$\begin{pmatrix} \sin\xi_G \\ \sin\chi_G \end{pmatrix} = -\frac{1}{2}\sqrt{2} \begin{pmatrix} \sin\xi_C - \sin\chi_C \\ \sin\chi_C + \sin\xi_C \end{pmatrix} \qquad (3.5)$$

To transform the global angles to the α and β angles use is made of formulae **(3.2)**.

As was mentioned before the sine signals coming from the secondary coils are transformed into a DC-voltage proportional to their amplitudes. How this was done in the old sensor is discussed in the following section.

3.1.2 OLD, ANGLE SENSOR.

In the old system the following setup was used to measure the angles:

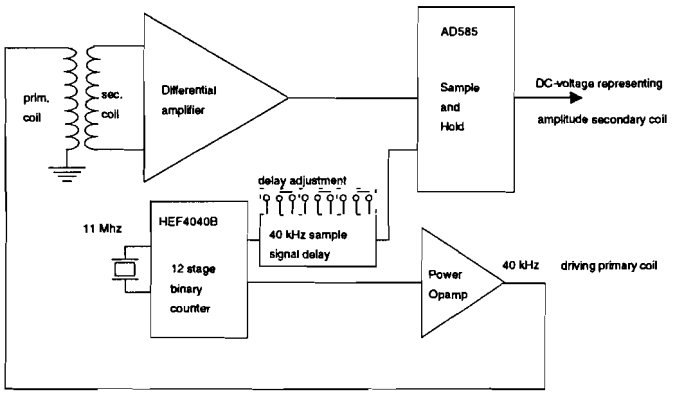

Figure 3.3 Measurement of angles in old system.

A crystal oscillator generates a block with a frequency of 11 Mhz. To get a frequency of 40 kHz this frequency is divided until a frequency of 40 kHz is reached and with a power opamp the block is transformed into a triangular waveform used as input to the primary coil. Due to the coupling between the secondary and primary coil, a voltage can be measured over the secondary coil. The amplitude of this voltage depends on the angle between the two coils. To transform the signal of the secondary coil into a dc-voltage a sample and hold circuit (AD585) is used. Because there is a phase delay between the secondary and primary coil voltage, the signal telling the AD585 to sample needs a phase delay to sample at the top (maximum SNR, eye-pattern) of the voltage over the secondary coil.

This setup has the following disadvantages:

1. A triangular waveform can be described by a fourier series:

$$\mathrm{tri}(f_0) = \sum_{n=0}^{\infty} \cos((2n+1)2\pi f_0 t) \qquad (3.6)$$

We not only get the desired frequency of 40 kHz but also multiple frequencies. These extra components can give distortion (when the group delay isn't equal) and (of minor importance) calculations are made difficult because if one wants to achieve the desired accuracy one needs to take into account the multiple frequencies and fault tracking becomes more difficult.

The remedy: use a sine wave.

The coils used can be represented by an inductance in series with a resistor: $L_C=L+R_L$. Therefore the following equations hold:

$$i_L = \frac{u_L}{j\omega L + R_L} \quad |i_L| = \frac{|u_L|}{\sqrt{(\omega L)^2 + R_L^2}} \quad \arg\{i_L\} = \arg\{u_L\} - \arctan\left(\frac{\omega L}{R_L}\right) \qquad (3.7)$$

The next remarks are all a consequence of foregoing equations.

A voltage source is used to drive the primary coil. This means that the phase of the current depends on the ratio of ωL to R_L . For an ideal coil (pure inductance, $R_L=0$) this ratio is ∞. So the current has a phase lag of 90°. One never has an ideal coil. For the mirror coil the following values were measured [1]:

	L	R	$\omega L/R$ ($\omega=2\pi 40\cdot 10^3$ [rad/s])
primary coil	449.9 µH	64.3 Ω	1.8
secondary coil 1	46.1 mH	875.6 Ω	13.2
secondary coil 2	48.4 mH	726.9 Ω	16.7

Table 3.1

In practice one usually tries to reach a $\omega L/R$ of about 20-50. As can be seen the $\omega L/R_L$ for the primary coil is more than 11 times smaller. (This gets even worse when using the new sensor because then we are bounded to a maximum frequency of 20 kHz. In which case $\omega L/R_L$ becomes 0.9!)

If the temperature changes R_L will change. The smaller the ratio of $\omega L/R_L$ the greater the phasechange between U_L and I_L. This brings us to the next disadvantage.

2. To use a sample and hold circuit makes the measurement very sensitive to timing errors. The secondary signal should be sampled at the top of the sine. But the sampling time is derived from the voltage applied to the primary coil. The current from the primary coil inducing a voltage in the secondary coil has however a phase that depends on the temperature so it is virtually impossible to sample on the right moments.

If the phase would stay constant one also deals with the sample-to-hold transition (time delay between signal saying: 'sample now' and the actual sampling time) of the ic used. The aperture delay is constant so it could be circumvented by adjusting the sampling time. But the aperture jitter is a true error source. If the signal has to be digitized with N-bits the maximum input signal frequency is equal to [Data sheets AD585]:

$$f_{max} = \frac{2^{-(N+1)}}{\pi \cdot (\text{Aperture jitter})} \qquad (3.8)$$

The aperture jitter is equal to 0.5 ns (typ.). With a min. of 16-bits as goal, would limit f_{max} to 4.9 kHz.

3. The sampling time is derived from the primary signal with the help of three jumpers. This means that the sampling time can't be adjusted continuously so it is never possible to place the sampling time on the peak time (or you must have a lot of luck. In which case I would advise to participate in a lottery.)

---

[1] Measurement was done with Wayne Kerr Automatic Component Bridge B605.

[2] If the frequency is chosen equal to 18 kHz (new electronics) the figures would become 0.8, 6.0 and 7.5 ,respectively.

4. There are no precautions taken to hold the amplitude of the primary signal at a constant level. If this amplitude changes the amplitude of the signal at the secondary coil will also change. The sensor will interpretate this as a change of the angle.

The remedy for the last three points: a combination of a circuit using the AD698 together with a current transformer and improving the primary coil, which means getting a better $\omega L/R_L$.

5. For a coil the maximum allowable continuously applied current density is equal to J=3 A/mm^2. As the wire used has a diameter of 50µm it follows that the maximum allowed current is 5.89 mA. The triangular wave has a V_{tt} of 16V. The rms value is equal to

$$\sqrt{\frac{1}{T}\int_0^T (16\cdot \mathrm{tri}(T))^2\,dt} = \sqrt{\frac{4}{T}\int_0^{T/4} (\frac{64}{T}t)^2\,dt} = \sqrt{85\tfrac{1}{3}} \qquad (3.9)$$

The amplitude of the impedance is equal to 130 Ω. The current is approximately 71 mA (rms). The allowed maximum is a factor ten smaller. To bring the current under the allowed maximum would mean a V_{tt} equal to 2.65 V. A lower voltage has the disadvantage that noise added has more impact on the signal-to-noise ratio.

The remedy: the new primary coil should have a higher impedance.

Besides these structural disadvantages the following faults were made in the implementation of the electronics:

1. The signals coming from the secondary coils were brought directly to the actual sensor with a flat cable.
2. The copper lines transporting the secondary signals on the print at the mirrors site to the flat cable connection picked up a lot of distortion. The copper lines were placed beneath the secondary coils. Even with the proper impedance one has to be aware of EMC problems because the coils form an open structure.

After this discussion of the shortcomings we will start with working out the remedies mentioned in the foregoing paragraphs.

3.1.3 THE NEW ANGLE SENSOR.

In the following section we try to answer the question: 'How do we have to change the primary coil to get a better $\omega L/R_L$?'. Section 3.1.2.2 reveals the new electronics measuring the angles the primary coil makes.

3.1.3.1 The primary coil.

The inductance of a coil can be approximated by the following formula [Kip]:

$$L_{appr} = c\frac{\mu_0\mu_r N^2\pi r^2}{h} \quad c = 2\cos(\alpha) \quad (3.10)$$

$$L_{appr} = 2\frac{\frac{1}{2}h}{\sqrt{(\frac{1}{2}h)^2 + r^2}}\frac{\mu_0\mu_r N^2\pi r^2}{h} \approx \frac{h}{r}\frac{\mu_0\mu_r N^2\pi r^2}{h} = \mu_0\mu_r N^2\pi r \quad (3.11)$$

The parameters are explained in Figure 3.4 and the values for the old coil are given in Table 3.2.

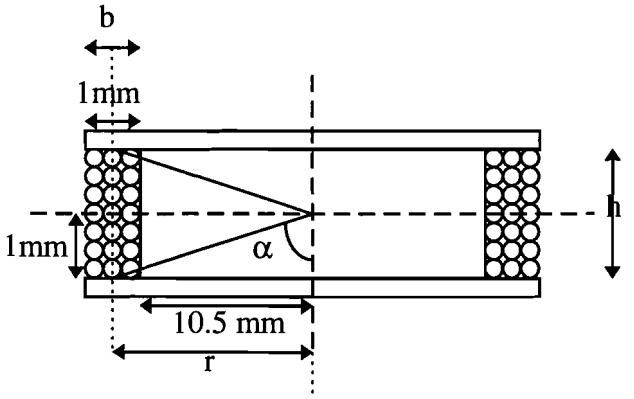

Figure 3.4 Primary coil.

c	$\frac{1\cdot10^{-3}}{\sqrt{(1\cdot10^{-3})^2 + (10.5\cdot10^{-3})^2}} = 9.481\cdot10^{-2}$
μ_0	$4\pi10^{-7}$ [Wb/Am]
μ_r	1 [3]
ρ	$1.7\cdot10^{-8}$ [Ωm]
N	100 windings
r	$10.5\cdot10^{-3}$ [m][4]
d	$50\cdot10^{-6}$ [m]
b	$1\cdot10^{-3}$ [m]
h	$2\cdot10^{-3}$ [m]

Table 3.2 Old coil parameters

If above values are used we find L_{appr}=412.7 μH. The relative error is (449.9-412.7)/412.7=9%.

The resistance can be approximated by:

[3] taking μ_r equal to one is an approximation, as the magnetic field lines travel a part of their trajectory through the steel semi sphere of the mirror.

[4] r is defined as radius celeron disc+0.5·thickness of coil. For this coil there are only two layers. Therefore $r=10.5\cdot10^{-3}+0.5\cdot2\cdot50\cdot10^{-6}$ is taken equal to $10.5\cdot10^{-3}$.

$$R_{appr} = \frac{\rho N 2\pi r}{\frac{\pi d^2}{4}} = \frac{8\rho N r}{d^2} \qquad (3.12)$$

R_{appr}=60.48 Ω. The relative error is equal to (64.33-60.48)/60.48=6.4%.

Both approximations are within 10% of the actual value. For the goal under consideration this is acceptable.

By dividing ωL_{appr} by R_{appr} and replacing N with $k\frac{b \cdot h}{\frac{\pi d^2}{4}}$ (k<1 is fillfactor coil)

the following equation is obtained:

$$\frac{\omega L_{appr}}{R_{appr}} \approx \frac{\omega k \mu_0}{2\rho} bh \qquad (3.13)$$

The variables determining this factor can be influenced in the following manner:

- ω equals 2π40 krad/s in the old configuration. As will become clear in the next section the new frequency is going down with a factor of about 2 because of the limitations of the electronics.

- k can be improved by taking thinner wires. One can imagine that if a thick wire is 'misplaced' this will consume more empty space.

- b and h can be increased to a limited extent due to mechanical constraints.

- Because copper is used ρ can only be improved by using silver. The improvement would be a factor $1.7 \cdot 10^{-8}/1.59 \cdot 10^{-8}$=1.069. The temperature coefficient is also improved by a factor $3.9 \cdot 10^{-3}/3.8 \cdot 10^{-3}$=1.026 (A lower temperature coefficient means improvement).

Because ω is limited to 2π20e3 it can be concluded from the previous analysis that the only way to improve $\omega L/R_L$ is the bh product. Before making a new primary coil for the actual mirror two test coils were made. The test coils had dimension as the primary coil on the mirror but the U-profile was taken 2mm×2mm.

d wire	#windings (theoretical)	#windings (practice)	relative %
50 μm	2073	700	34
100 μm	509	130	25

Theoretical:

	L	R	ωL/R (ω=2π18·10³ [rad/s])
d=50 μm	22.2 mH	437.9 Ω	5.7
d=100 μm	764.4 μH	20.3Ω	4.3

Practical:

	L	R	$\omega L/R$ ($\omega=2\pi 18\cdot 10^3$ [rad/s])
d=50 μm	18.9 mH	424.6 Ω	5.1
d=100 μm	663.4 μH	14.1 Ω	5.3

In spite of a lower $\omega L/R$ value we decided to choose d=50 μm because of the following reasons:
1. Impedance is greater this means a higher voltage can be applied to the coil without exceeding the maximum allowable current.
2. Because the number of windings is much larger the deviation between the test coils and the coil as it will be produced for the actual mirror will be relatively smaller .

The implementation yield the results shown in Table 3.3.

parameters	value
h	$2.3\cdot 10^{-3}$
b	$1.275\cdot 10^{-3}$
#windings	750
fillfactor	50.22%
L	21.2 mH
R_L	470.3 Ω
$\omega L/R_L$	5.4
mass	$+1\cdot 10^{-3}$ kg

Table 3.3 Measured results of new coil.

h×b became 2.3 mm × 1.275 mm. Nonetheless $\omega L/R_L$ became 5.4. The explanation for this is that the increase in fillfactor (from 34% to 50%) compensates the decrease in bh (from 4 mm^2 to 2.93 mm^2).

Compared to the case were the frequency was 40 kHz an improvement of a factor 3.1 was obtained if compared with 18 kHz a factor 6.8 was reached.

Because of the extra mass the system is becoming slower. To calculate the consequence the next section is devoted to the calculation of the inertia.

3.1.3.2 Influence on inertia.

The semi sphere is made of a steel[5] half sphere around which a ring of celeron is placed. The ring contains three holes to connect to connect the twaron strings. Radial to the holes three springs ($k\approx 0$) are attached. Two springs are connected to the primary coil. The half sphere for the capacitive measurement of the air gap is supplied with a sine through the third spring. To make space for the windings the inner material (marked in Figure 3.5) has to be removed. Because the gaps are only on three places the ring still holds its structure.

[5] The semi sphere can be made of a material (e.g. glass, can be non-conducting) on which a layer (conducting) is damped or of a conducting massive material. However, a massive steel semi sphere is (a lot) easier to fabricate. On top of that there is always the possibility of the semi sphere hitting its bearing in which case the damped layer would be damaged. It would take a few weeks to a month to repair the semi sphere. As consequence the choice was made to make the semi sphere of massive steel.

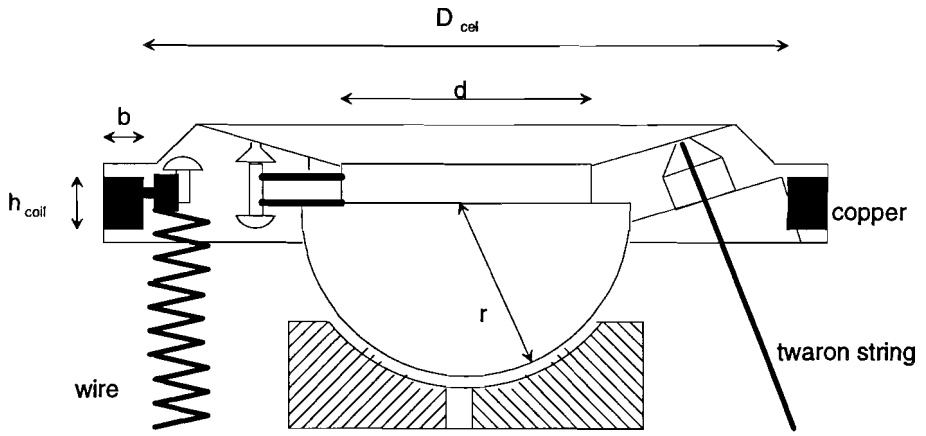

Figure 3.5 Side view of primary coil.

For the calculation of the inertia the semi sphere is divided into three parts: sphere, disc and coil with inertia [Zorge, Sass, Pol] of, respectively:

$J_{b,xy}=4/15\cdot\pi\cdot\rho_b\cdot r^5$
$J_{d,xy}=\pi/4\cdot\rho_d\cdot h_{cel}\cdot(D_{cel}^2-d^2)\cdot\{(1/16)\cdot(D_{cel}^2+d^2+(4/3)\cdot h_{cel}^2)+y_c^2\}$
$J_{c,xy}=\pi/4\cdot\rho_c\cdot h_{coil}\cdot((D_{cel}+b)^2-D_{cel}^2)\cdot(1/16)\cdot((D_{cel}+b)^2+D_{cel}^2+(4/3)\cdot h_{coil}^2)$

These are the inertia's about an axis in the X_G,Y_G-plane. The inertia about the Z_G-axis of the sphere, disc and coil are, respectively[6]:

$J_{b,z}=4/15\cdot\pi\cdot\rho_b\cdot r^5$
$J_{d,z}=\pi/4\cdot\rho_d\cdot h_{cel}\cdot(D_{cel}^2-d^2)\cdot(1/8)\cdot(D_{cel}^2+d^2)$
$J_{c,z}=\pi/4\cdot\rho_c\cdot h_{coil}\cdot((D_{cel}+b)^2-D_{cel}^2)\cdot(1/8)\cdot((D_{cel}+b)^2+D_{cel}^2)$

The inertia's of the disc are more an approximation than a calculation. The celeron-disc has a 'wave'-form that is approximated with a disc that stops where the coil begins.

With the values of the old and new coil shown in the table below

[6] In previous simulations and calculations the inertia about the Z_G-axis was taken equal to the inertia in the X_G,Y_G-plane. See e.g. [Noten, Goossens]. The values for ϕ' (rotation around Z_G-axis) will decrease in the simulations of [Noten]. This effect is called turn up. During experimenting with the mirror no 'visual' turning up was noticed.

		old coil	new coil
ρ_b	density steel	$7.7 \cdot 10^3$ [kg/m^3]	
ρ_d	density celeron	$1.4 \cdot 10^3$ [kg/m^3]	
ρ_c	density copper	$8.9 \cdot 10^3$ [kg/m^3]	
r	semi sphere radius	$5.0 \cdot 10^{-3}$ [m]	
D_{cel}	disc diameter till coil	$2.14 \cdot 10^{-2}$ [m]	
D	outer disc diameter	$2.4 \cdot 10^{-2}$ [m]	
d	inner disc diameter	$8.0 \cdot 10^{-3}$ [m]	
h_{cel}	celeron height[7]	$2.0 \cdot 10^{-3}$ [m]	
h_{coil}	coil height	$2.0 \cdot 10^{-3}$ [m]	$2.3 \cdot 10^{-3}$ [m]
b	coil	$1.0 \cdot 10^{-4}$ [m]	$1.275 \cdot 10^{-3}$ [m]
y_c	distance from center of gravity disc to point of rotation	$1.0 \cdot 10^{-3}$ [m]	

Table 3.4 Old and new half semi sphere parameters.

the following values are obtained:

[kg·m^2]	old coil	new coil
$J_{b,xy}$	$2.0 \cdot 10^{-8}$	$2.0 \cdot 10^{-8}$
$J_{d,xy}$	$3.0 \cdot 10^{-8}$	$3.0 \cdot 10^{-8}$
$J_{c,xy}$	$3.5 \cdot 10^{-9}$	$5.6 \cdot 10^{-8}$
$J_{tot,xy}$	**$5.4 \cdot 10^{-8}$**	**$10.6 \cdot 10^{-8}$**
$J_{b,z}$	$2.0 \cdot 10^{-8}$	$2.0 \cdot 10^{-8}$
$J_{d,z}$	$5.7 \cdot 10^{-8}$	$5.7 \cdot 10^{-8}$
$J_{c,z}$	$3.2 \cdot 10^{-11}$	$6.3 \cdot 10^{-9}$
$J_{tot,z}$	**$7.7 \cdot 10^{-8}$**	**$8.3 \cdot 10^{-8}$**

Table 3.5 Old and new inertia's of semi sphere.

As can be seen the inertia in the xy-plane has doubled. This means that the mirror is becoming a factor $\sqrt{2}$ slower ($E=1/2 \cdot J \cdot \omega^2$). The inertia around the z-axis is increased with ±10%. This is to our advantage because this will decrease the turn up noted by [Noten].

3.1.3.3 The electronics.

The foregoing circuit could be improved by measuring the current through the primary coil and deriving the sampling time with an analogue phaseshifter from the measured current. But we would still suffer from the other disadvantages.

The angle measurement is an inductive measurement. Another measurement based on the same principle is found with LVDT's. There are ic's available giving a voltage proportional to the position of the core. The following section discusses the AD698 LVDT signal conditioner as used with an LVDT.

[7] This is a mean value. The celeron disc has a 'wave'-form. The part were the coil is seated is somewhat thicker.

3.1.3.3.1 The AD698.

In Figure 3.6 a block diagram of the AD698 together with an LVDT (Linear Variable Differential Transducer) is shown.

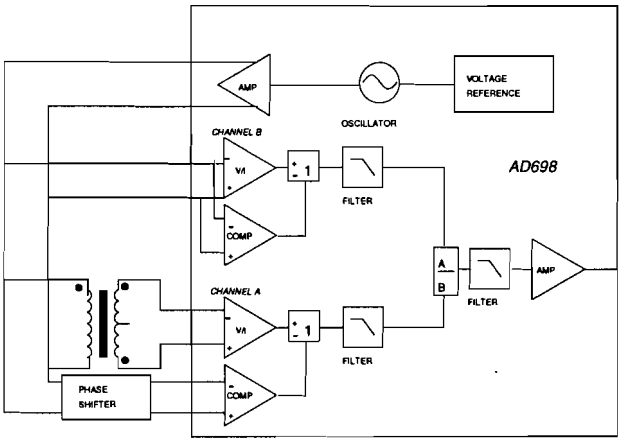

Figure 3.6 Schematic overview of AD698 connected to an LVDT.

The LVDT is an electromechanical transducer. Its input is the mechanical position of the core, and its output is an ac voltage proportional to core position.

The series-opposed connected LVDT transducer consists of a primary winding energized by an external sine wave reference source and two secondary windings connected in the series opposed configuration. The output voltage across the series secondary increases as the core is moved from the center. The direction of movement is detected by measuring the phase of the output.

The AD698 has a sine wave oscillator and power amplifier to drive the LVDT. And decodes LVDTs by synchronously demodulating the amplitude modulated input (secondary), A, and a fixed input reference, B. The later one should be the voltage as it is applied to the primary coil. The ratio of the demodulated signals is a measure for the position of the core. Division by the amplitude of the signal applied to the primary coil (channel B), cancels out drift in the amplitude of the drive oscillator.

One can easily see that the mirror system can replace the LVDT as the amplitude modulation in the mirror system is taken care of by tilting the primary mirror. We still have to solve a problem. As mentioned before the AD698 is able to cancel out drift in the signal applied to the primary coil. If that coil has a $\omega L/R_L$ of 50 there is a negligible difference between the applied voltage and the voltage over the inductance of the coil. In our system this isn't the case.

The following section starts with presenting the solution to this problem and will finish with the discussing of the actual angle sensor.

3.1.3.3.2 The angle sensor.

With the current transformer, see Figure 3.8 (upper part), the current through the primary coil is measured. This current is then transformed into a voltage that is amplified with part of the

circuit to a voltage of $i_{prim}R_{L,appr}$. $R_{L,appr}$ is the resistance of the coil as measured at 27^{o} celsius or the mean temperature at which the circuit is going to be used. This voltage is subtracted from the voltage measured over the primary coil. In equations:

$U_L=j\omega Li_{prim}+R_Li_{prim}$
$V_{out}= j\omega Li_{prim}+R_Li_{prim}-R_{L,appr}i_{prim}=j\omega Li_{prim}+(R_L-R_{L,appr})i_{prim}$

The last term still depends on the temperature but has become approximately a factor 20 smaller. This voltage is then used as input to channel B and $R_{L,appr}\cdot i_{prim}\cdot$gain is used as input to the phase shift network.

In Figure 3.8 the sensor for one secondary coil is shown. It consists of the AD698, a Butterworth low-pass filter, fixed voltage regulator and the coil voltage sensor.

As can be seen in Figure 3.6 the AD698 'contains' three filters. A filter at the output of each demodulator (C2 and C3) and a filter at the output stage (C4 and C_{shunt}). In Figure 3.7 the right picture shows the output voltage ripple vs. filter capacitance the left part shows the transfer function of the AD698 (without additional C_{shunt}). C2,C3 and C4 were chosen equal to 0.033 μF giving a 3-dB bandwidth of 3 kHz. With C_{shunt} chosen equal to 10 nF a ripple of 0.4 mV rms exists. This is approximately 1.13 mV peak-to-peak (sine approximation). If 16-bits at an interval of -10 to +10 V has to be reached one needs a ripple which has a peak-to-peak amplitude of 0.305 mV. Therefore an additional filter is necessary.

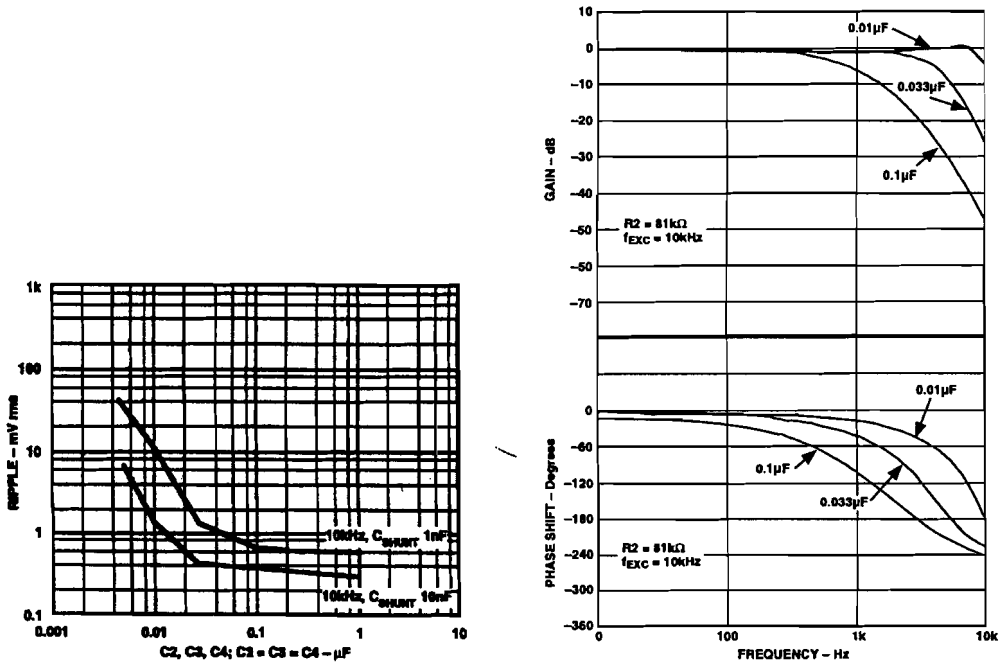

Figure 3.7 Output ripple vs. output capacitance (left). Transfer function (right).

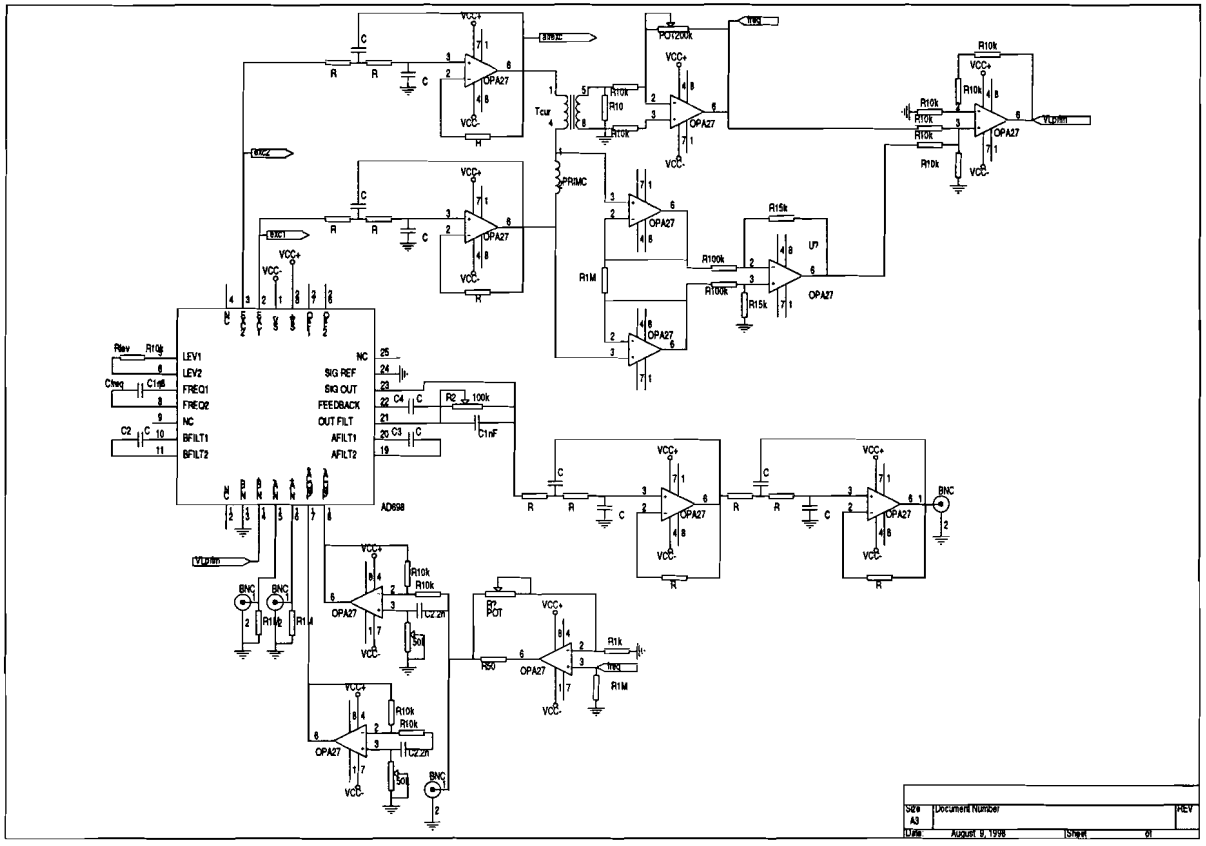

Figure 3.8 Implementation of master angle sensor.

In the specifications only the phase and gain characteristics were given without the additional C_{shunt}. In first instance the sensor was implemented without the C_{shunt}.

To start with a 6^{th} order Butterworth low pass filter with a bandwidth of 3 kHz was used. From measurements it turned out that a 4^{th} order low pass filter gives enough attenuation. The high frequency (> 3 kHz) components have a larger amplitude but they don't increase above the components below the 3 kHz.

As power source an AC-DC voltage source was used. But when analyzing the output of the sensor with the SA it was noticed that components at frequencies 50, 150, 250, 350,... were generated. It isn't possible to use a filter at the output of the sensor to attenuate these frequencies.

To test whether the secondary coil picked up a 50 Hz signal a high pass filter was placed between the secondary coil and the input to the AD698. However the frequencies were still there and no attenuation had taken place. Therefore it could be concluded that the frequencies are due to the voltage source. To increase the line regulation a voltage regulator was used but this didn't solve the problem either. When batteries are used the problem is cancelled out entirely. (Remark: These components have such a low amplitude that they can't be distinguished from the other noise if only the oscilloscope is used.)

Till now we have discussed the operation of one primary coil with one secondary coil. But the actual system has two secondary coils. This can be solved by using the setup as shown in Figure 3.12. The AD698 of Figure 3.8 is used as master, the AD698 of Figure 3.12 is configured as a slave by connecting the exc1 and exc2 outputs of the master to the lev1 and lev2 of the slave with 15 kΩ and connecting freq1 and freq2 together. (As shown in the next section a third AD698 is also implemented as a slave.).

In the next section the parameters of the sensor will be discussed.

3.1.3.3.3 Parameters of sensor.

The parameters to be discussed below were measured with a special setup consisting of a primary (attached in a turnable holding) and secondary coil having an L of 19.0 mH and 20.0 mH and a R of 412.3 Ω and 413.5 Ω, respectively. The primary coil has almost the same values as the primary coil used in the mirror. The secondary coil was made according to documentation belonging to the mirror. The measurement of the L and R values showed that the actual secondary coil has a smaller inner radius (L and R of test coil are smaller). Because of lack of time the measurements were done with the coil made. The fact that the measurement is done with this setup will only degrade the performance of our sensor because in the mirror system there less gain needed to use the full scale output of the sensors. If not mentioned otherwise, the parameters hold for the master and slave sensor.

- **resolution**, was tested using an oscilloscope. The angle between the primary coil and secondary coil was varied (with the help of the test table) between +25 and -25 degrees. The output of the sensor was measured with an oscilloscope using the AC-input mode and with a time scale of 10 ms. The peak to peak variations stay well between **5 mV**. The majority of the variations stays between 2 mV.

- besides the resolution, which is a measure for fast variations, the **slow variations** were measured. With a universal multimeter having an IEEE bus and an accuracy of 5 decades data acquisition was automated. In Figure 3.9 the outcome of this experiment is shown.

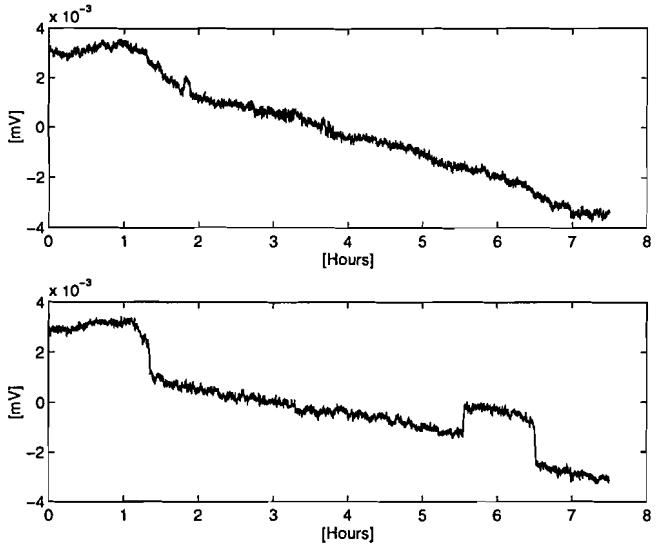

Figure 3.9 Output of angle sensors during a measurement of 7½ hours.

The output of the sensor decreases 1 mV/hour. This is clearly a temperature effect. If it is caused by the circuit itself and/or the increase in room temperature during the day should be clearified by doing the same measurement under conditioned circumstances. If the cause is the circuit, a longer measurement should clarify if this decrease goes on till the AD698 shuts off (temperature monitor) or an equilibrium is reached. Irrespectively of the outcome off these experiments a temperature stabilisation will be needed in the final system.

- **input-output relation**. The test table that was to our disposal should have a resolution of 1/60 degree. During testing it was noticed that there was some slack. Therefor the angle-voltage relation was measured between -25 and +25 degrees and a resolution of 1 degree.

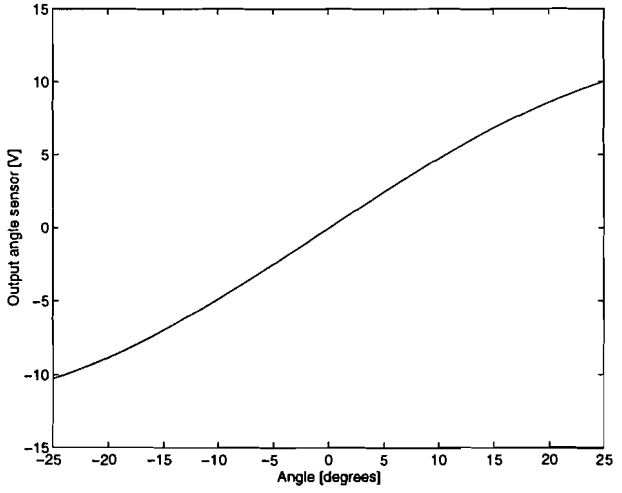

Figure 3.10 Input-output relation.

In the mirror system the input-output relation will be more nonlinear. Because of the half-semi sphere made of steel the magnetic field lines will be 'more non-symmetric' as seen from a plane through the mirrors surface.

- **sensitivity**. The sensitivity is equal to $\partial angle/\partial V$. To get a very rough indication one could make an approximation with $\Delta angle_{tt}/\Delta V_{tt}=(50/180\cdot\pi)/20=$**43.6 µrad/mV**. The resolution of 5 mV would be equal to 218 µrad.

- **transfer function between angle and output angle sensor**. The modulation of the carrier frequency is normally caused by tilting the primary mirror. The angle of the test table couldn't be adjusted electrically so one could consider to determine the transfer function with the actual mirror. However, the measurement is only reliable over the frequency range over which the height controller is able to keep the air gap constant. This would limit our measurement to about 50 Hz. To modulate the frequency electronically the setup of Figure 3.11 was designed:

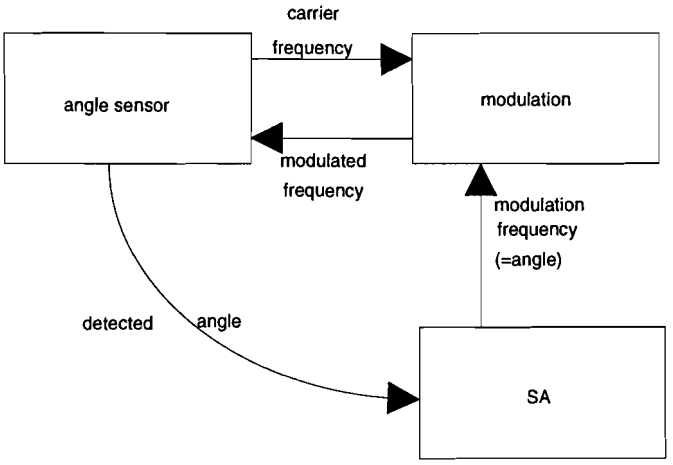

Figure 3.11 Transfer function measurement.

For the angle measurement the AD698 is used completely differential. This would mean that two modulators would be necessary. We had already trouble finding one modulator. Therefore the measurement was done with the height sensor (will be discussed in the next section) based on the AD698 in the common mode. The transfer function will be the same, but for the measurement only one modulator is needed.

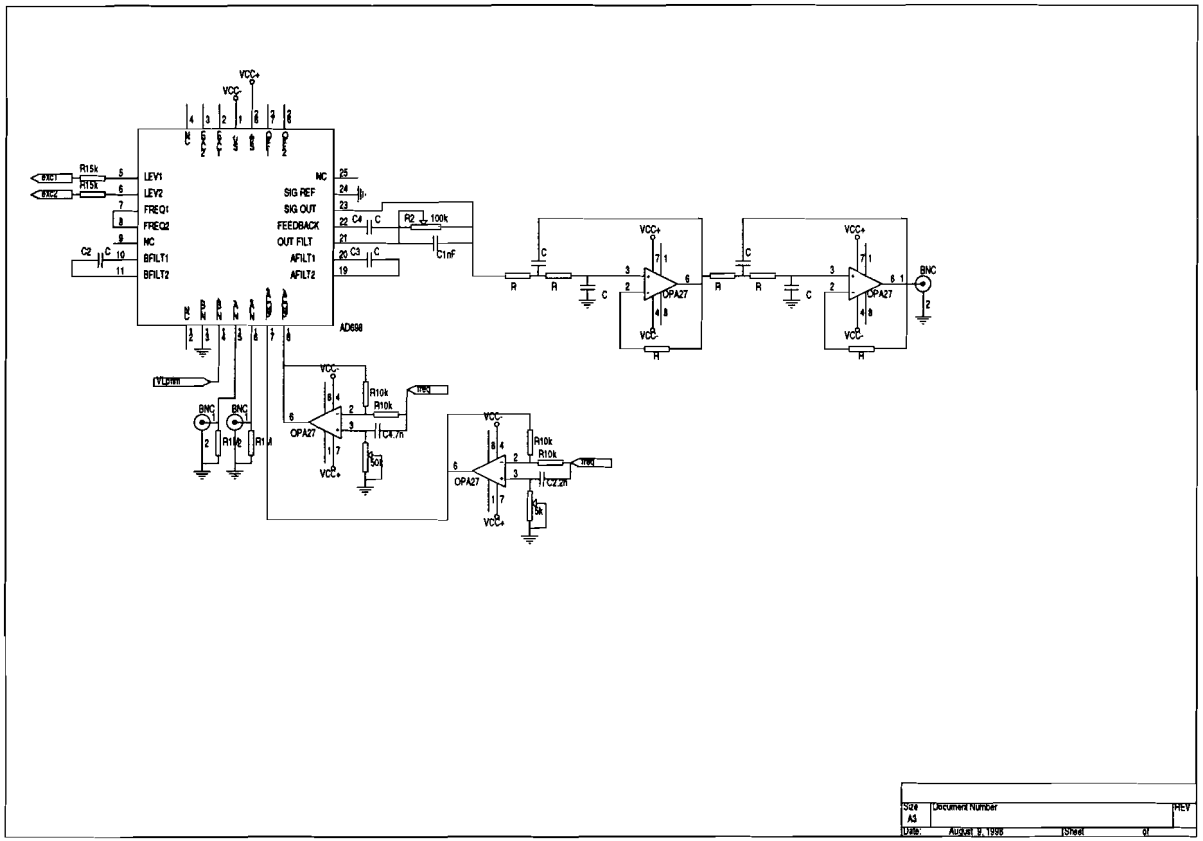

Figure 3.12 Implementation of slave.

With this setup the following result was obtained (4th order low pass Butterworth filter with C_{shunt}=1 nF):

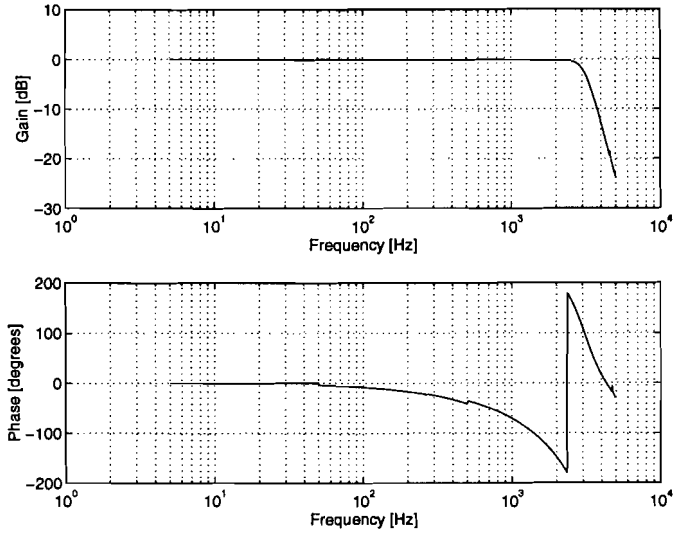

Figure 3.13 Transfer function of angle sensor.

300 Hz	0 dB
3.1 kHz	-3 dB
300 Hz	-24 degrees
2.3 kHz	-180 degrees

Table 3.6 Sensor attenuation and phase delay.

The phase delay is caused primarily due to the filter used. As it is of primary importance to have a good representation of the angle at the frequencies in the bandwidth a flat gain is needed. A Butterworth filter has a maximal flat gain, if the filter had been optimized for phase the gain wouldn't be flat and/or the -3dB point would decrease.

The sensor has a 3-dB bandwidth equal to 3.1 kHz and a resolution of 218 μrad. With these values the scanning mode can be implemented. For a measurement of the position of the retroreflector (retroreflector not moving) one wants a sensitivity equal to 10 μrad. This is possible by placing a low-pass filter with a very low bandwidth (e.g. 10 Hz) after the sensor. All noise will be filtered out. However there is one important constraint. The slow variations shouldn't exceed the 10 μrad. The slow variations with this sensor implementation exceed this value. If the goal of 10 μrad has to be reached these variations should be brought down, e.g. by temperature regulations of the electronics and mirror system.

Besides the angle sensor the mirror system needs an air gap sensor.

3.2 THE AIR GAP SENSOR.

3.2.1 THE OLD SENSOR.

To control the air gap height we need to measure the height of the mirror above the seat. Because both mirror and bearing seat are made of metal, this can be done contactless by measuring the capacitance of the air gap between the semi sphere and bearing seat.

A schematic overview of old system measurement is shown below.

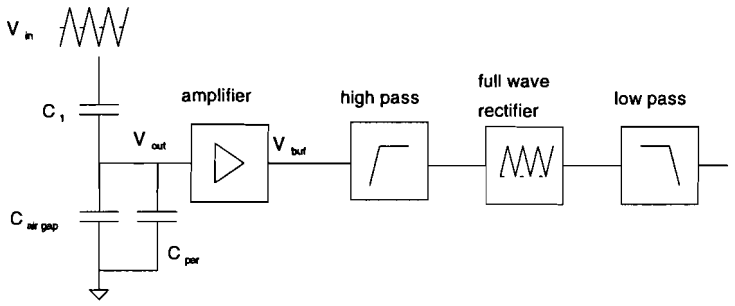

Figure 3.14 Schematic overview of old measurement system.

A triangular wave (frequency 40 kHz) is used as input to the sensor. The series connection of C_1 (1.8 pF) with C_{airgap} (parallel with C_{par} the parasitic capacitances) forms a divider. Because C_{airgap} depends on the air gap the amplitude of V_{div} is a measure for the height. With the amplifier the signal is amplified and an output is created with low impedance. The high-pass filter is used for attenuating of 50-Hz and 100-Hz components. The rectifier in combination with the low pass filter creates a DC-signal depending on the amplitude V_{out}.

With the old sensor there were a few problems described by Looymans. In summary these problems were:
1. To get the desired accuracy during implementation an extra low pass filter was placed after the low pass filter already there. The bandwidth of this low pass filter was lowered till the resolution of the sensor was equal to 2 mV (This extra low pass filter had the break frequency at 20 Hz and a roll of rate of -40 dB/dec!). Resulting in a closed loop bandwidth of about 20 Hz for the controller of [Looymans].
2. The amplitude of the generator needs to be very stable, otherwise these variations are seen as variations of the air gap height. These variations have a gain equal to the sensitivity.

3.2.2 THE NEW SENSOR.

Two sensors were implemented and tested. The first sensor developed was based on the previous measurement system, thus still suffering from the second problem. The second sensor made use of the AD 698.

3.2.2.1 Sensor based on old measurement system.

The major change is the replacement of the output filter by a 6^{th} order lowpass Butterworth filter. The total sensor is shown in Figure 3.16.

The circuitry can be divided into three parts:

1. Rectifier. Instead of the active rectifier used in the previous implementation the AD630 was used. An active rectifier uses the signal itself to switch. The AD630 needs an additional

sine (at the clk input) that has to be in phase with the signal of which the absolute value is wanted. The clk input can be derived from the sine applied to the input of the height sensor. It needs to be attenuated twice and because there is a slight phase difference between the attenuated signal and the signal input to the rectifier a phase shifter needs to be added.

2. Phase shifter. This is the same network as used in the angle sensor.

3. Butterworth filter. A 6^{th} order low pass filter with a 3-dB frequency of 3 Khz was implemented. 3 kHz was chosen because in this way the attenuation is negligible for the closed loop bandwidth of about 300 Hz. A 6^{th} order filter was used because a 4^{th} order filter doesn't provide enough attenuation and an 8^{th} order doesn't bring any improvement over a 6^{th} order.

As can be seen there is no high-pass filter placed in front as with the old sensor. There are two reasons for this:
1. C_1 together with the input of the amplifier form already a high pass filter.
2. The attenuated 50 Hz or 100 Hz (DC-power source) are chopped by the rectifier with a frequency of 18 kHz the low pass filter will average the chopped pieces.

For this sensor the following parameters were measured:

- **resolution**, was determined with an oscilloscope. The peak to peak variations stay well between **5 mV**. The majority of the variations stays between 2 mV.

- besides the resolution, which is a measure for fast variations, the **slow variations** were measured. With a universal multimeter having an IEEE bus and an accuracy of 5 decades data acquisition was automated. In Figure 3.15 the outcome of this experiment is shown.

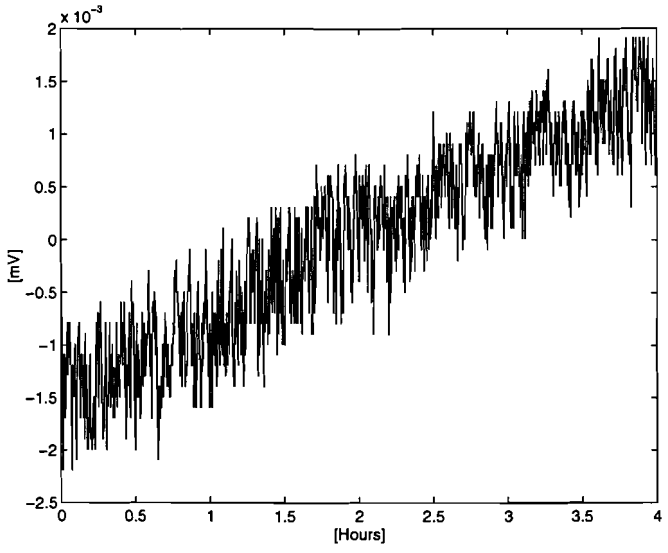

Figure 3.15 Output of air gap sensor during a period of 4 hours.

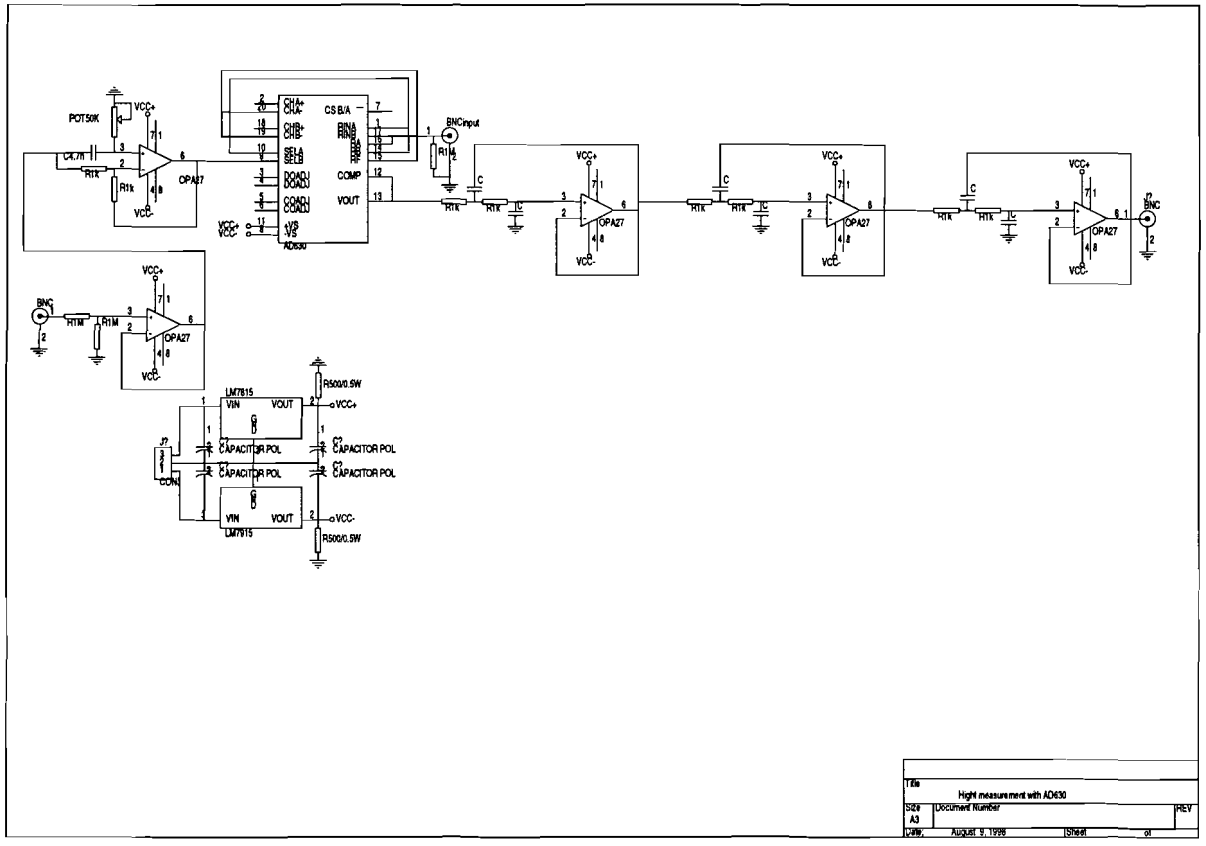

Figure 3.16 Implementation of air gap sensor based on old sensor principle.

An increase of 1mV/Hour can be seen. This is a temperature effect due to the rising of the circuit temperature.

- **input-output relation**. The relation between the voltage and the actual air gap has not been determined. The necessity is low because during calibration a constant reference voltage is determined that is used for the control. So there is only zero control, no tracking regulation is needed.

- **sensitivity**[8]. to measure the sensitivity the actual air gap is needed. This was calculated with the following relationship [Zorge]:

$$C_{airgap} = \ln(\cos(\alpha_e))\frac{\varepsilon_0\varepsilon_r\pi 4R^2}{d} \qquad (3.14)$$

The meaning of the parameters is explained in Figure 3.17.

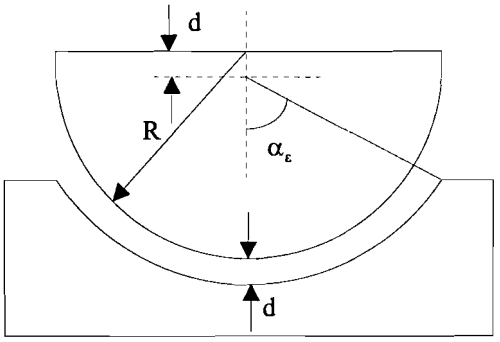

Figure 3.17 Parameter explanation of air gap capacitance formula.

C_{airgap} can be calculated because (see also Figure 3.14):

$$V_{buf} = \frac{K_{buf}C_{shunt}}{C_{shunt}+C_{airgap}+C_{par}}V_{in} \qquad (3.15)$$

with C_{shunt}=1.8 pF and C_{par}=5 pF. V_{buf} and V_{in} can be measured [9]. K_{buf} is equal to the buffer gain. With the measured data, depicted in Figure 3.18, a sensitivity was calculated of **11.4 nm/1 mV**.

[8] This sensitivity was measured with a gain of 11 at the mirror PCB. With this gain the sensor has an output voltage of about 4 Volt in the 'reference position'. The same voltage is generated by the implementation based on the AD698. It is of course possible to change the sensitivity by changing this gain. The value has been calculate here to give an indication of the numbers.

[9] V_{buf} is measured instead of V_{out} because the probe and the air gap capacitance are both in the order of pF.

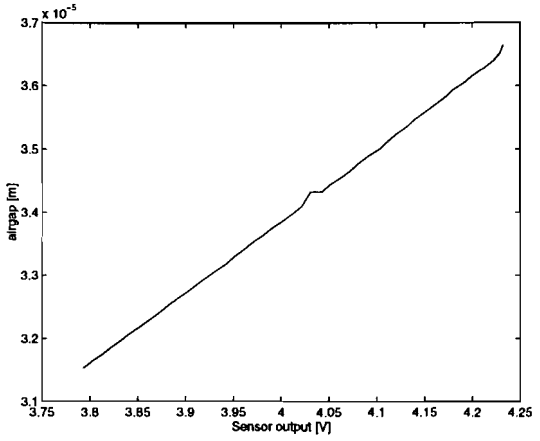

Figure 3.18 Air gap versus sensor output (based on AD630) around equilibrium.

As the noise was about 5 mV **the sensors resolution is 57 nm**. If this sensitivity is enough (this depends on a combination of point 2.1 of section 2.3 and the accuracy of the angle measurement in the total measurement setup) has to follow from calculations on which H. Theunissen is working on.

- **transfer function between air gap and sensor output**. For determination see angle sensor.

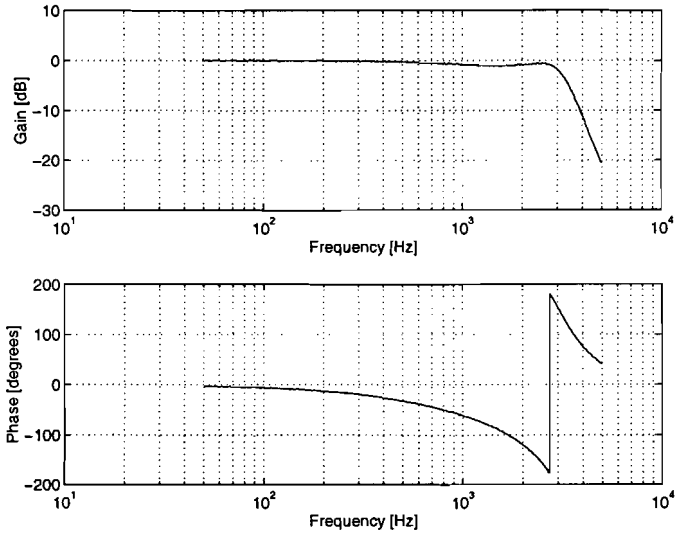

Figure 3.19 Transfer function air gap sensor based on AD630.

300 Hz	-0.14 dB
3 kHz	-3 dB
300 Hz	-18 degrees
2.6 kHz	-180 degrees

Table 3.7 Sensor attenuation and phase delay.

Below an overview of the parameters is given.

Sensitivity	11.4 nm/1 mV
Resolution	57 nm
Transfer function	- 3 dB bandwidth 3 kHz

Table 3.8 Parameter overview air gap sensor based on AD630.

The bandwidth is enough for building an air gap controller and the resolution is comparable to the resolution of the sensor discussed in the next section. However this sensor doesn't solve the problem of amplitude drift in the excitation voltage. The next sensor is capable of annihilating this drift.

3.2.2.2 Height sensor based on AD698.

In the previous section the AD698 was extensively discussed. If it is driven as a slave in the same way it was used to measure one angle it can also be used as a height sensor. The great advantage that we are able to annihilate any fluctuations in the amplitude of the generator (master AD698).

In Figure 3.22 the implementation of this sensor is shown.

For this sensor the following parameters were measured:

- **resolution**, was determined with an oscilloscope. The peak to peak variations stay well between **5 mV**. The majority of the variations stays between 2 mV.

- besides the resolution, which is a measure for fast variations, the **slow variations** were measured. With a universal multimeter having an IEEE bus and an accuracy of 5 decades data acquisition was automated. In the outcome of this experiment is shown.

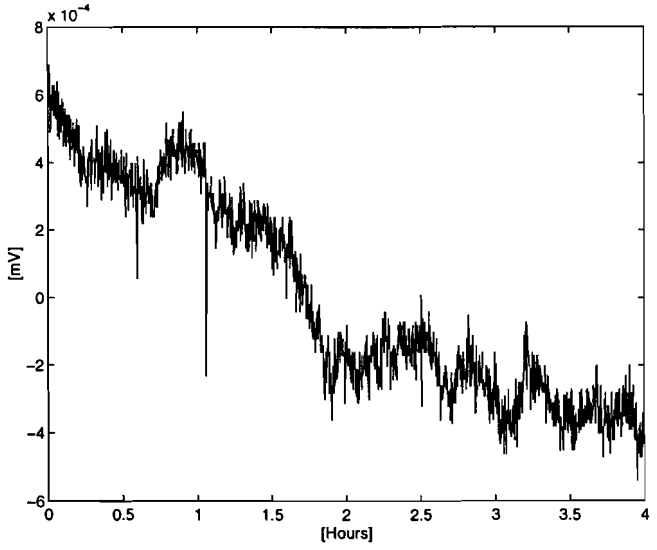

Figure 3.20 Output of air gap sensor during a period of 4 hours.

This circuit based on the AD698 only shows a decrease in temperature of 0.25 mV/Hour. This could be caused by the fact that the measurement was done on a day with a lower temperature and the temperature was more stable. The angle sensor could also be more

sensitive for temperature because the coil parameters depend stronger on temperature than the air gap capacitance. Further experiments are needed to pinpoint the reason.

- **input-output relation**, see implementation of air gap sensor based on old principle.

- **sensitivity**. Again data was collected around the equilibrium.

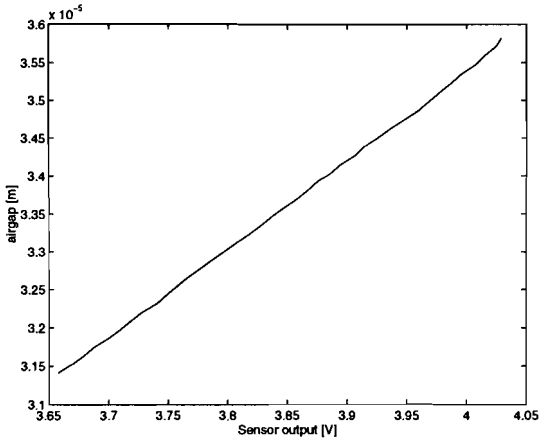

Figure 3.21 Air gap versus sensor output (based on AD698) around equilibrium.

From Figure 3.21 it can be concluded that the **sensitivity is 12.2 nm/1 mV**. So the **resolution** of 5 mV is equal to **61 nm**.

- **transfer function**, see angle sensor. The implementation based on the AD630 has more attenuation and phase delay. The combination of the filtering of the AD698 together with the 4th order Butterworth is obviously a better combination then the 6th order Butterworth filter used in the AD630 implementation.

Below the parameters are shown together.

Sensitivity	12.1 nm/1 mV
Resolution	61 nm
Transfer function	- 3 dB bandwidth 3.1 kHz

Table 3.9 Parameter overview air gap sensor based on AD698.

Before moving on to the PSD sensor a section will be devoted to a discussion of the mutual influence of the angle and height sensor.

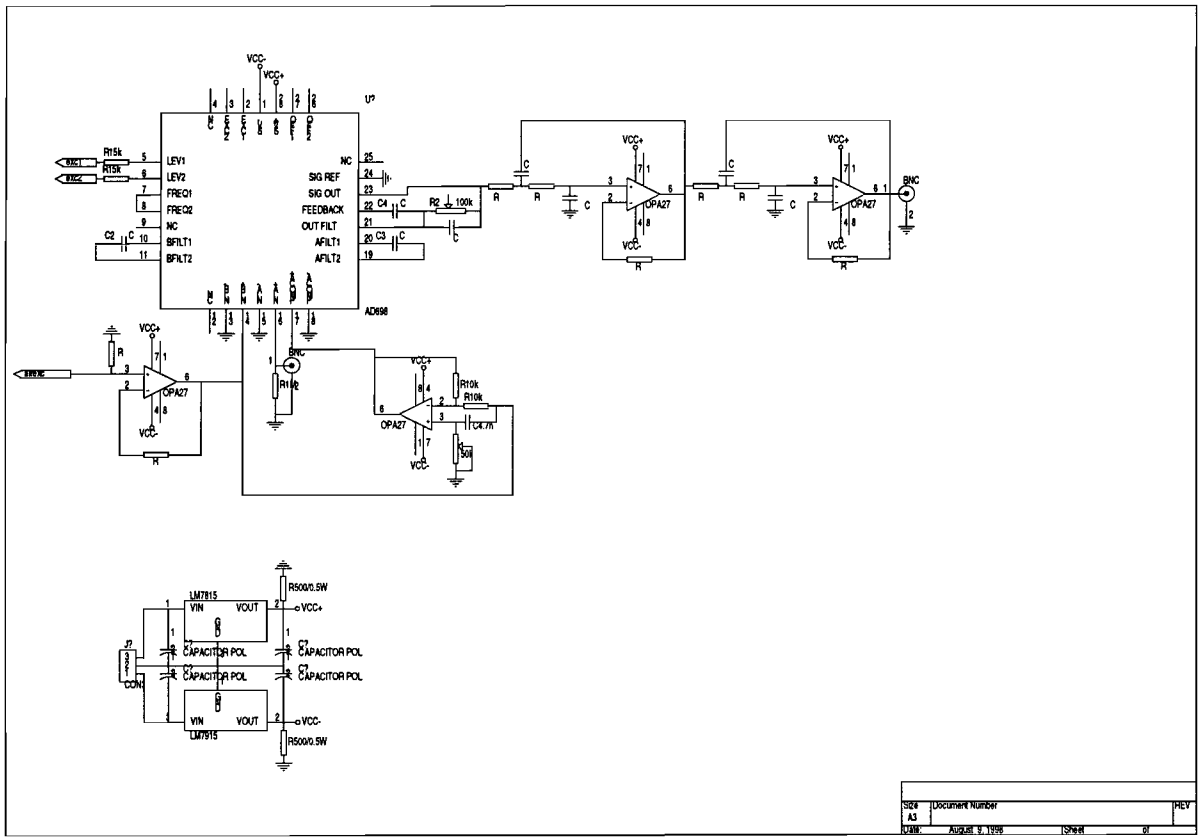

Figure 3.22 Implementation of air gap sensor based on AD698.

3.3 MUTUAL INFLUENCE ANGLE AND AIR GAP SENSOR.

The angle measurement is based on the magnetic part of an (open) electromagnetic field and the air gap measurement is based on the electric part of an electromagnetic field (sited between two plates). A concern therefore is the parasitic coupling between the primary coil and the air gap and how this depends on the tilting of the primary coil.

An overview of the different parasitic capacitances is shown below.

In the left part of Figure 3.23 two capacitors are shown. The wire is connected to the PCB via a clip. At the PCB the clip is connected with a nut. For the analysis this is divided into two parallel capacitances.

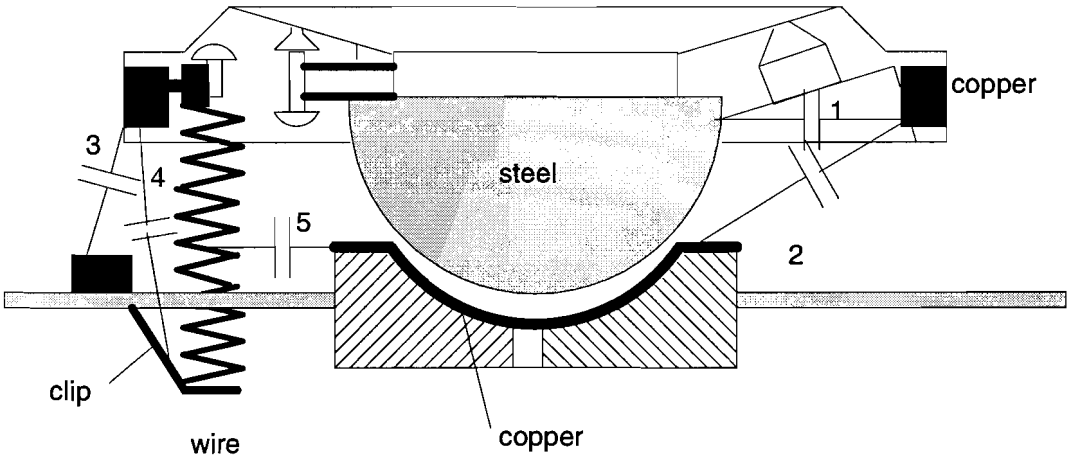

Figure 3.23 Schematic overview of parasitic capacitances.

In Table 3.10 a worst case approximation (A is taken largest, d smallest) is made of the values.

	parasitic capacitance	A [m^2]	d [m]	$C_{par}=\varepsilon_0 \cdot A/d$	$f(\alpha,\beta)$[10]
1	primary coil↔steel semisphere	$1 \cdot 10^{-4}$	$5 \cdot 10^{-3}$	$18 \cdot 10^{-12}$	--
2	primary coil↔semisphere copper	$22 \cdot 10^{-6}$	$5 \cdot 10^{-3}$	$4 \cdot 10^{-14}$	+-
3	primary coil↔nut	$2 \cdot 10^{-5}$	$5 \cdot 10^{-4}$	$36 \cdot 10^{-12}$	++
4	primary coil↔wire connection	$16 \cdot 10^{-6}$	$1 \cdot 10^{-3}$	$14 \cdot 10^{-12}$	++
5	wire↔air bearing copper	$1 \cdot 10^{-6}$	$1 \cdot 10^{-3}$	$8.85 \cdot 10^{-15}$	+-
C_{air} lays around 30 pF with the reference as used the controller of Chapter 4.					

Table 3.10 Approximation of parasitic capacitances.

[10] -- means minor dependence and ++ major dependence, α and β are the tilting angles.

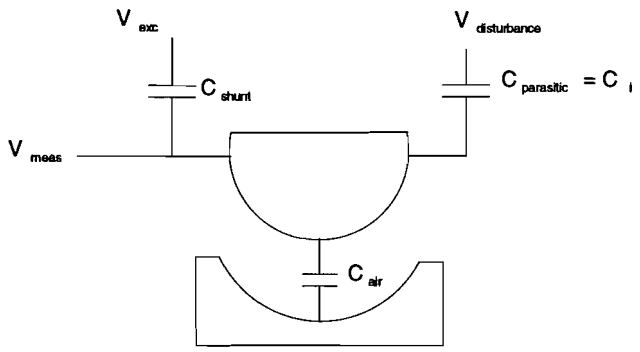

Figure 3.24 Searching for parasitic capacitance.

In Figure 3.24 a schematic overview shows how the air gap voltage is changed by the parasitic capacitances. Capacitance 1 belongs to the sought category. 2 is connected to ground and is therefore of no influence to the measurement (C_{par} so small that it's influence on the coil voltage can be neglected). Capacitances 3 and 4 are parallel to the wire. In the drawing this wire is connected to the primary coil. So in the shown case these capacitances will not influence the air gap measurement. But there are three wires in total! One of the other two can be neglected for the same reason just mentioned. However, the third connection is connected to the semi sphere and the parasitic capacitances 4 belonging to this wire will certainly influence the measurement. Capacitance 3 isn't there for this connection because the nut is smaller and made of plastic. Capacitance 5 is connected to ground and is only of influence as a voltage divider as it is connected to the wire. The influence will be small because of the small value of C_{par}.

The major influence of the air gap to the primary coil is via the capacitances 1 and 2. Because the impedance of capacitance 2 is 450 times the impedance of capacitance 1 the whole steel voltage (which is kept constant for disturbances lower than the bandwidth of the controller) is added to the primary coil voltage. But this shouldn't cause any problem. As was explained in chapter 3 the AD698 measures the amplitude of the voltage over the primary coil. The secondary voltage is divided by the measured voltage to annihilate any variations in the primary coil voltage.

Which options are available to lower the parasitic capacitances:

- The upper side of the PCB should be used as a grounded shield.

- Making the wire connections (nut and clip) to the PCB smaller!

- Currently the AD698 is connected differential for the angle measurement. It is possible to make the connection common (see Appendix C). In this way one wire (to the primary coil) can be connected to ground. This gives two options to lower the capacitic coupling. The first option is obtained when the 'outer' layer of the primary coil is grounded (neglecting the R_{wire}). The second option is to enclose the primary coil in a grounded shield. This shield should have sliced openings to prevent the generation of Eddy currents.

When the AD698 is used in the common mode one needs to solve an existing problem in another way. The AD698 needs three inputs: the voltage over the primary coil (+Bin,-Bin), the voltage over the secondary coil (+Ain,-Ain) and a frequency in phase with the later signal (+Acomp,-Acomp). These six pins are all situated beside one another (see Figure 3.8). Due to cross-over a signal is measured over the secondary inputs even when this is not connected. If the AD698 is used in differential mode it is possible to adjust the amplitude of one of the

inputs to minimize the differential signal. If the AD698 is used in common mode, one could eliminate the cross-over signal if the B-input is 180° delayed in relation to the A-input. It would then be possible to place a 'capacitor' (e.g. two twisted wires) between Bin and Ain to minimize the total cross-over signal. (The exact nature and dimensions of the cross-coupling isn't known yet. Still waiting on response of Analog Devices.)

Besides lowering the capacitic coupling one could also think of using different frequencies for air gap and angle measurement.

As was discussed extensively in the previous sections the primary coil has a low $\omega L/R_L$ so one wants a high frequency. Because the upper limit is 20 kHz the only solution would be to give the air gap measurement a lower frequency (Using a higher frequency is only possible if the old principle is used. Giving the disadvantage of amplitude drift). However new problems are introduced when using this solution. Because the cross coupling is still there, additional filtering will be necessary introducing more phase shift. As it will never be possible to suppress the components entirely it will give extra distortion in the sensor. When lowering the frequency the impedances increases and becoming more susceptible for pickup of e.g. 50 Hz components.

Measurements should be done to quantify the influence of the tilting on the air gap measurement. If this is too high one should first try to lower the parasitic capacitances before using different frequencies.

To be able to implement the tracking mode a position sensing detector is needed.

3.4 POSITION SENSING DETECTOR

The position sensing detector (from now on abbreviated as PSD) is an opto-electronic device which converts an incident light spot into continuous position data. One can imagine that it calculates the center of gravity of the incident light. Therefore it is independent of the absolute light intensity.

The PSD consists of two parts. The actual sensor that detects the light and generates currents and the electronics processing these signals.

In the Figure 3.25 two dimensional PSD structure and its equivalent circuit is shown. The photoelectric current generated by the incident light flows through the device and can be seen as two input currents (one through each resistance) and two output currents. The distribution of the output currents show the light spot position of one dimension (Y), and the distribution of the input currents the position in the other dimension (X).

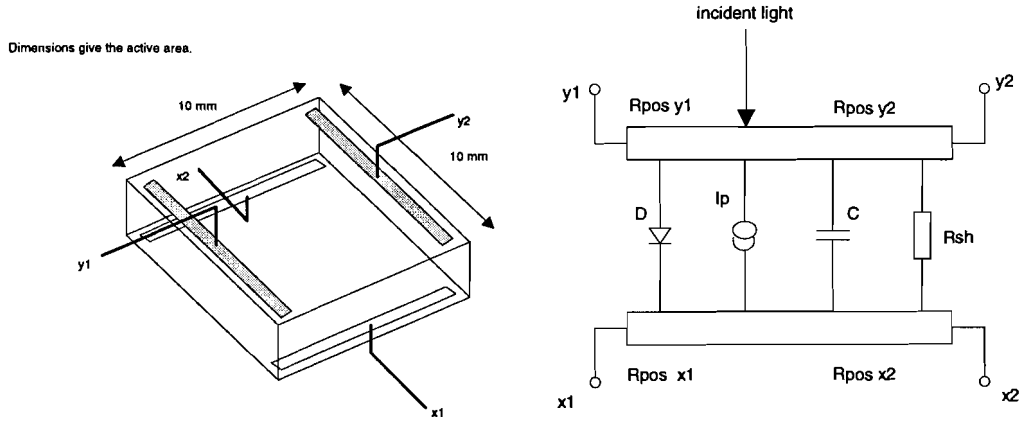

Figure 3.25 Two dimensional PSD structure and equivalent circuit.

With the currents the electronics calculate the positions x and y as follows:

$$\frac{X2-X1}{X2+X1}=\frac{x}{L} \qquad \frac{Y2-Y1}{Y2+Y1}=\frac{y}{L} \qquad (3.16)$$

Because X2+X1 (and Y2+Y1) is a measure for the absolute light intensity in this direction the absolute light spot intensity does not affect the light spot position.

In the practical setup we have to pay attention to the following items:

1. The PSD may receive a maximum of 30000 W/m^2 light intensity. The spot has a radius of approximately 1 mm. Therefore the light intensity is bounded to a maximum of $\pi(1\cdot10^{-3})^2\cdot30000=94$ mW. The current laser used has a light intensity of 1 mW. With the setup as shown in Figure 1.1 only a quarter of the total power is received by the PSD. The light intensity of the laser has to be taken such that the maximum allowable intensity is received by the PSD to maximize the signal to (outer) noise (other light falling on the PSD) ratio.

2. The output current/watt light as function of the wavelength is shown in Figure 3.26. Three PSD's are shown, each optimized for different types of lasers.

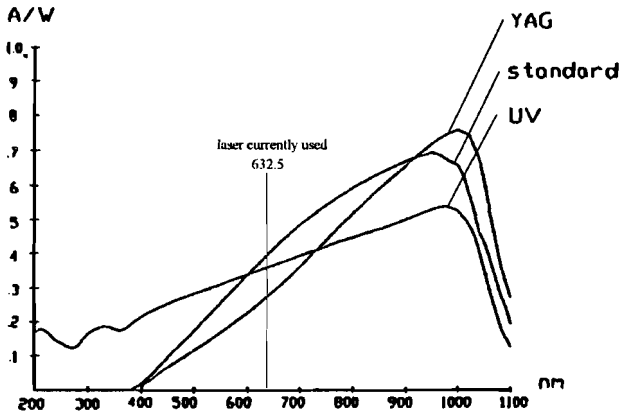

Figure 3.26 Output current/watt light as function of the wavelength.

As can be seen the PSD is also sensitive for day-light and light received from TL light (visible light ranges from about 400 to 700 nm). This noise introduces two effects:

2.1 The disturbing light doesn't hit the PSD with equal intensity because the light has a gradient in its intensity. If e.g. the laser beam hits the PSD (in this example a one dimensional PSD) at about a third of its length (black strip) and the light-'noise' puts more weight (blacker) at the left of it the center of gravity will be pulled to the left. One can imagine that if the measurement system is displaced or the measurement takes several hours this will influence the measurement. It would mean that for each new measurement a calibration would be necessary.

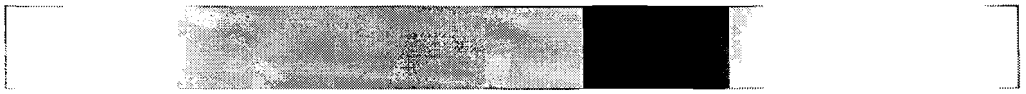

Figure 3.27 Lightnoise distribution. Black=laser.

2.2 Even when the light noise would have equal intensity one gets a kind of binary situation if the light would contain TL-light because the TL switches.

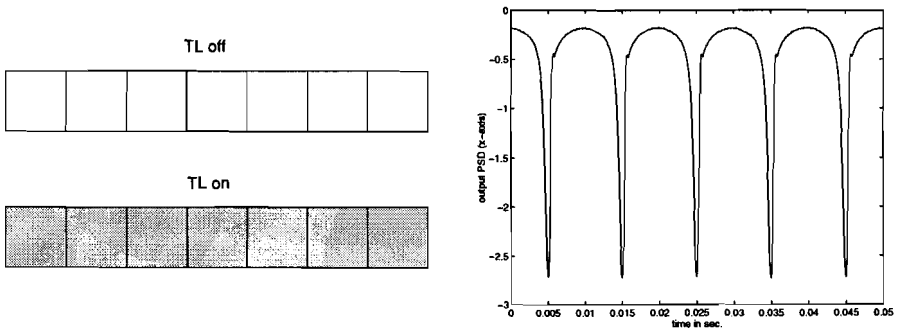

Figure 3.28 TL-switch effect.

In Figure 3.28 the output of the PSD (one-axis) is shown when placed in front of a TL. Every 1/100 sec the TL switches of for a short period of time. In practice this switching won't be such extreme. But one sees a 100 Hz sine superposed on the x-,y-coordinate.

How both noise sources will influence the measurement will strongly depend on the distribution of the disturbing light and the light intensity. If noise is present, attention has to be paid to the non-linearity introduced by (**3.3**):

$$\frac{(X2+\Delta)-(X1+\Delta)}{(X2+\Delta)+(X1+\Delta)} = \frac{X2-X1}{X2+X1+2\Delta} \qquad (3.17)$$

The noise can be attenuated by placing an optical bandpass filter in front of the PSD. This filter has to have a center frequency that is as close as possible to the frequency of the laser used (The PSD used has to have its optimum also as close as possible to this frequency.). It is important to choose the laser-frequency far enough from the disturbing frequencies to ensure that the attenuation in the stop-band of the optical filter is high enough and the sensitivity of the PSD is low enough to suppress the disturbances to a level sufficient to reach the accuracy needed for the PSD.

3. When placing the bandpass filter in front of the PSD an additional effect will occur, shown in Figure 3.29. A part of the laser beam will reflect on the surface of the PSD giving multiple reflections in combination with the optical bandpass filter.

For normal uncoated silicon 32% of the light is reflected. SITek's AR coating reflection is (minimum) 2% optimized for the wavelength region around 860 nm. Because of the accuracy needed for PSD measurement in the steady state mode this effect can distort the measurement too much. If the laser beam falls in perpendicular the reflections will fall together with the actual laser beam giving no coordinate distortion.

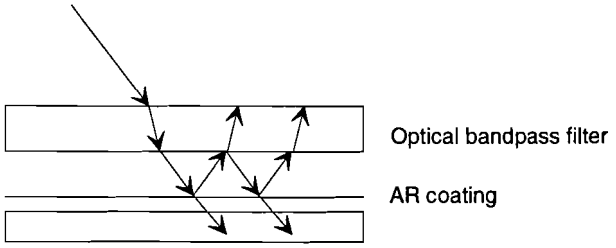

Figure 3.29 PSD with optical bandpass filter.

4.

For the parameters of this sensors it is important to distinguish between the sensor that detects the light and the electronics converting the current into a position. In Table 3.11 the light sensors parameters are shown.

Parameter	Light sensor (SiTek 2L10SP)
Non-linearity	±0.3%
Thermal drift	20-40 ppm/°C
Resolution	0.1 ppm[11]
Rise time	0.2 μs
Spectral response	Figure 3.26 (normal)

Table 3.11 PSD parameters.

Currently the OT-300DL amplifier (producer ON-TRAK photonics inc.) is used. The input sensitivity can be set to 10^{-3} to 10^{-5} A/V, the non-linearity is equal to 1% and the channel to channel tracking is 1%. At this point it isn't known if these parameters fulfill the need. (E.g. Philips makes better boards for processing the currents coming from the light sensor.)

In the previous chapters the mirror system itself and the sensors were discussed. The next two chapters are devoted to the discussion of the controllers combining the mirror system and sensors in the classical closed loop configuration.

[11] Every 7°C increase in temperature will cause the dark current to double. If the light intensity is low this will influence the resolution.

4. THE TRACKING MODE.

In the tracking mode two controllers are working independently. The air gap controller will be discussed first, followed by a description of the angle controller.

4.1 THE AIR GAP CONTROLLER.

4.1.1 MEASURING THE TRANSFER FUNCTION.

[Looymans] derived a model for the air gap, see chapter 2. With a spectrum analyzer the transfer function was measured. The calculated model parameters were adjusted to match the theory with the practical measurement.

The coherence plot of Looymans measurement is repeated below in Figure 4.1.

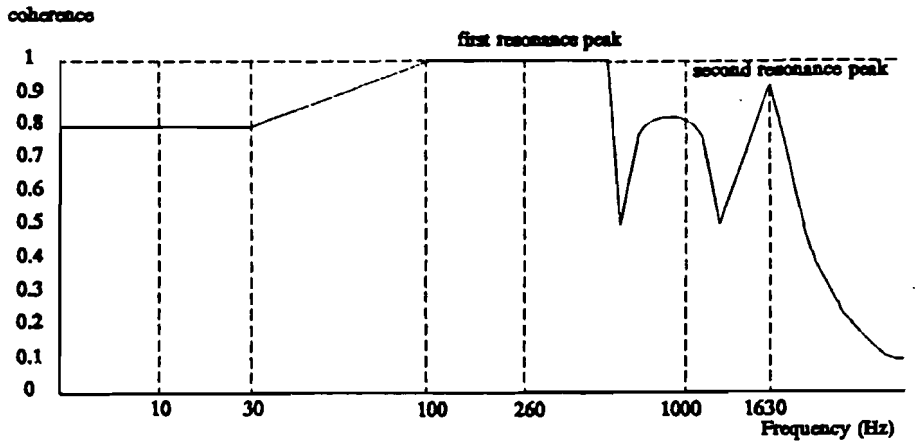

Figure 4.1 Coherence plot [Looymans].

As can be seen there are some regions were the coherence is significantly below 0.95.

The spectrum analyzer is able to calculate the pole-zero pattern belonging to the measured transfer function. The calculated transfer function has however only meaning if the coherence is greater than 0.95. To use the measurement to adjust the zero/poles of the theoretical transfer function and build a controller based on this model is therefore questionable.

With another setup of the measurement, see Figure 4.2, we are able to fulfill the coherence constraint.

When the spectrum analyzer (SA) operates in the servo mode (with the option log sin) it measures the response of the mechanical filter (the Device Under Test), in our case the mirror system, to a sine excitation. The frequency of the excitation sine takes a number of discrete values (lines/decade) between the bounds given by the user.

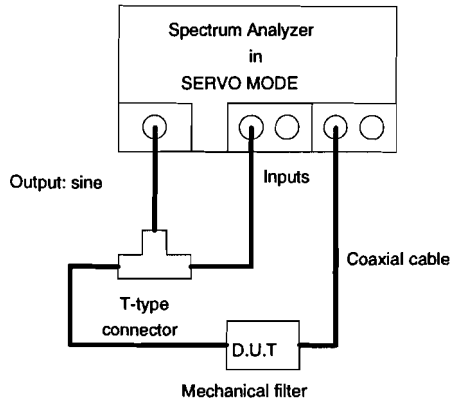

Figure 4.2 Transfer function measurement setup.

With this setup the air gap transfer function was measured for different air gaps to find out whether the transfer function, in particular the resonance frequencies, depend on the working point.

The working point can be adjusted by setting the pretension strings tighter and/or setting a DC-level on the actuators. The calculation of the air gap belonging to this setting can be done in the same way as in section 3.2.2.1.

It is possible to add a DC level with the help of the SA during the measurement. However at the same time a sine (with varying frequency) will be imposed on this level. This makes measuring of V_{buf} difficult (the amplitude of the carrier is modulated by the varying air gap because SA excitates the actuator input with a sine). It is easier to build an adder and to superimpose the DC-level with a DC-source. In this way the measurement of the air gap can be done without the SA running.

In Figure 4.3 and Figure 4.4 the measured transfer functions are shown for various air gaps as indicated in Table 4.1.

Measurement	Air gap [μm]
1	62.0
2	56.8
3	51.8[12]
4	33.5
5	32.5
6	31.5
7	28.7
8	27.8

Table 4.1 Air gaps for measurement.

[12] After this measurement the pretension string was adjusted, this caused a considerable decrease in the air gap.

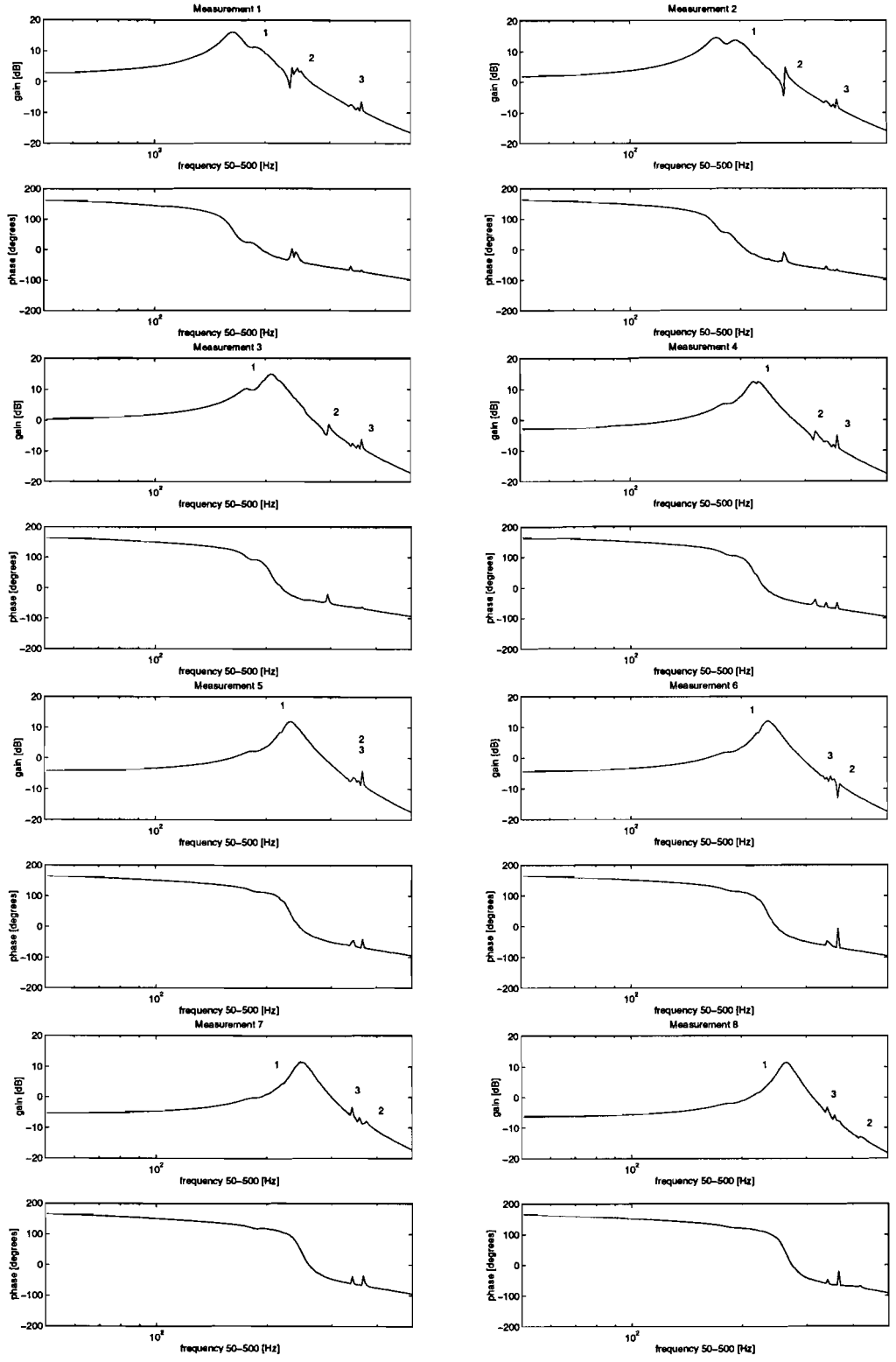

Figure 4.3 Measured air gap transfer function 50-500 Hz.

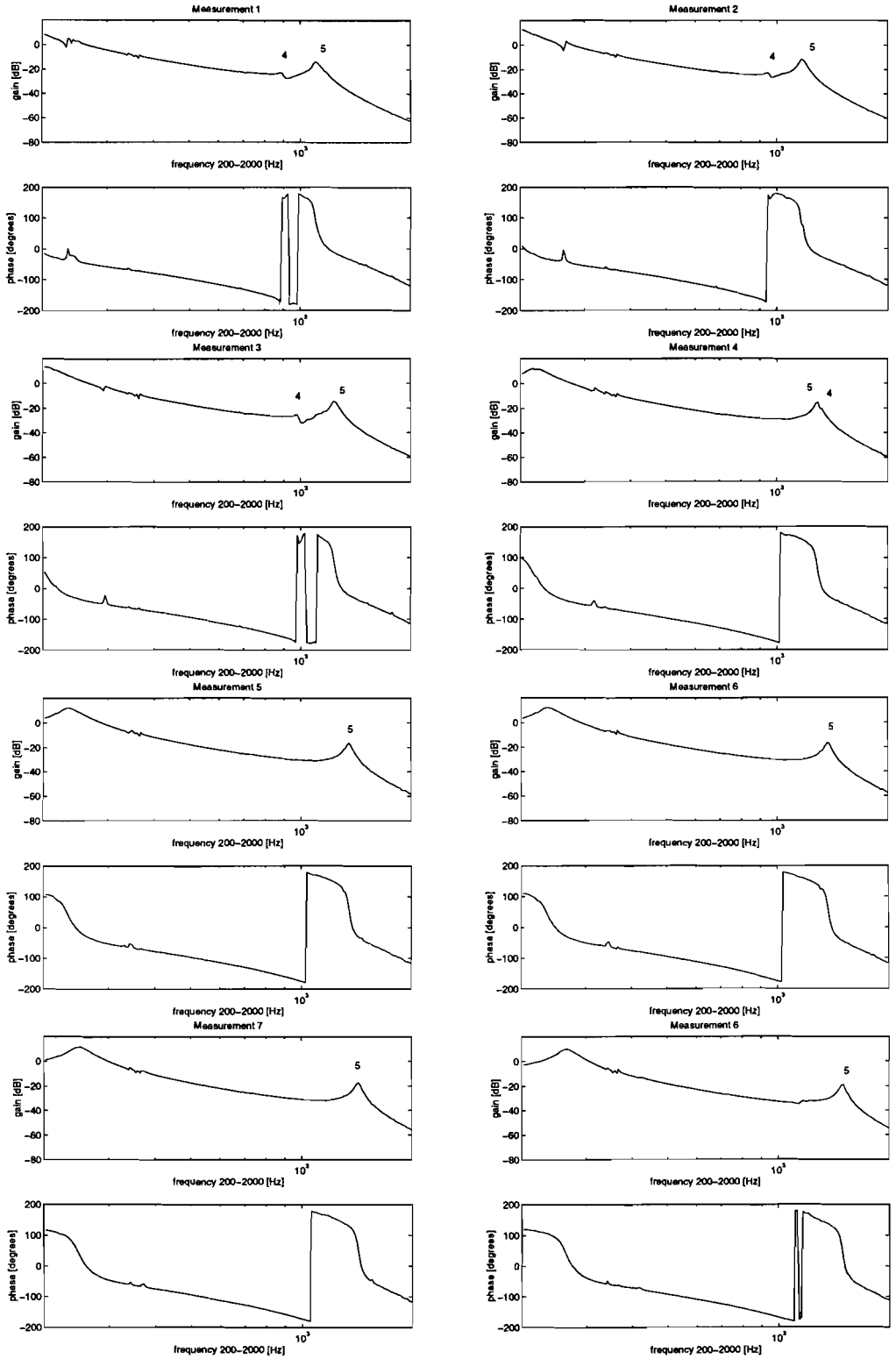

Figure 4.4 Measured air gap transfer function 200-2000 Hz.

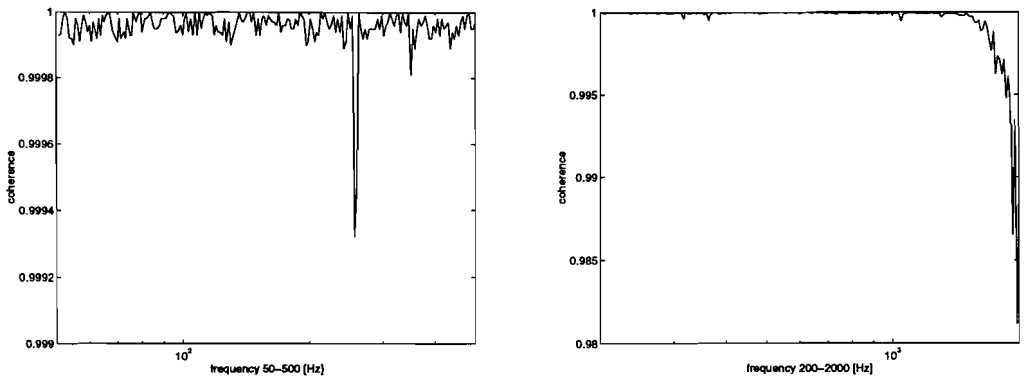

Figure 4.5 Coherence plot belonging to measurement 1.

The coherence function belonging to measurement 1 is shown in Figure 4.5 (the coherence functions of the other measurements show the same behavior). As can be seen the coherence stays well above 0.95.

Remark: as can be seen the air gap has a minus sign. In the theoretical transfer function shown in (**2.7**) there is no 180 degree phase delay. Because h is defined from a reference position downwards an increase in h results in a decrease in the air gap.

There are in total 4 areas containing resonance frequencies.
- The resonance frequency of area 1 consists of two frequencies. The theoretical model predicted only one frequency here, see Figure 2.4.
- The resonance frequencies turning up at about 250 Hz, area 2, in measurement 1 move towards higher frequencies when the air gap becomes smaller. At the same time the amplitude decreases. These resonance's aren't predicted by the theoretical model.
- Area 3 consists of three small peaks. These peaks are not influenced by the air gap. (This is also the reason why the measurement method was changed. Because with the measurement method Looymans used they aren't measured.)
- The resonance peak of area 4 moves towards higher frequencies when the air gap becomes smaller after measurement 4 this peak seems to have disappeared.
- Area 5 contains a resonance peak predicted by the theoretical model.

If the measured transfer function is compared with the calculated transfer function as shown in Figure 2.4 the model didn't predict several resonance frequencies. What is the cause of these resonances?

The theoretical model assumes complete, triple symmetry. In practice this won't be the case. Compared to the symmetric case this gives 5 extra modes of freedom resulting in extra resonance peaks.

Another difference when compared to the model is the rest position of the mirror. In the rest position the mirror faces the wall and not ceiling. The modeling is done lateral to the rest position of the mirror. But in the actual system forces are also acting perpendicular on it. Gravity is pulling the steel hemisphere downwards, the twaron strings are pulling the hemisphere up & down (depending on the string) and the air is pushing the mirror from all sides. To test whether these forces are the cause of the resonance frequencies the transfer function was measured with the mirror turned 90 degrees. The outcome is shown below.

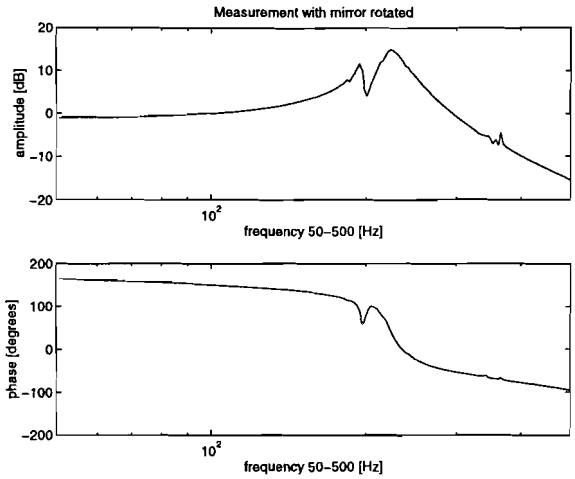

Figure 4.6 Measured transfer function with mirror system rotated 90 degrees.

As can be seen the resonance frequencies are still there. Therefore this theory isn't correct.

The resonance frequencies could also be the result of transversal resonance frequencies of the twaron strings in combination with the actuator coil and the pretension string. No test was developed yet, to test this theory.

The resonance frequencies of area 3 are caused by the actuators because these aren't influenced by an air gap variation. They could depend on the actuator air pressure. This dependence hasn't been tested. It would be advisable to do this.

As the air gap control is a constant reference control one needs to choose a working point. The working point was chosen equal to measurement 8. The setpoint was made with the help of the mechanical connections determining the tension of the pretension strings.

With Testlab the data from the SA was transferred to the PC and the separate measurements were combined to one file and used to calculate the transfer function with the invfreqs function of Matlab. The result is shown below.

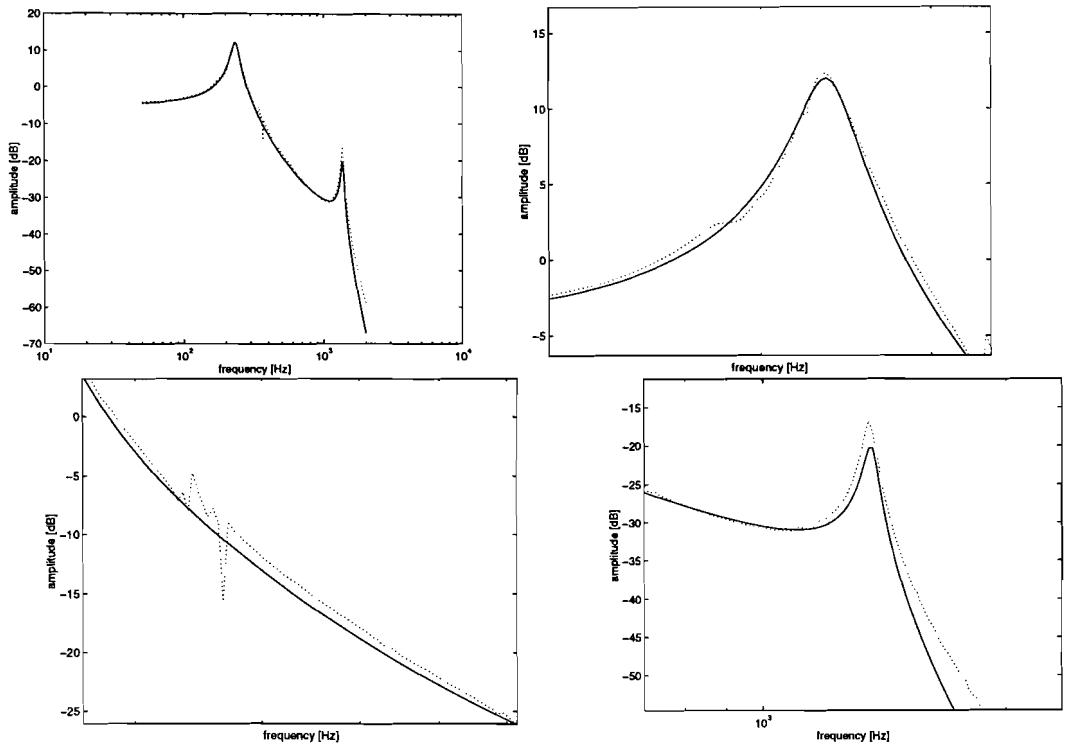

Figure 4.7 Measured transfer function (dotted) and identification (solid).

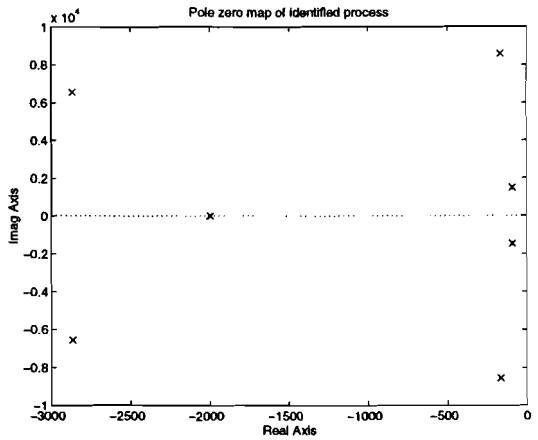

Figure 4.8 Pole zero map of identified process.

As can be seen the three resonance peaks of area 3 aren't modeled. However, the controller to be designed should not 'break down' on these frequencies.

4.1.2 CONTROLLER DESIGN AND IMPLEMENTATION.

The PID controller should have a zero-steady state error. This means that the control should contain at least one pole in the origin. The controllers bandwidth will be limited by the need of enough attenuation around 350 Hz to suppress the three resonance frequencies.

As PID controller design is more an art than a science several controllers were developed and tested. The choice was made for implementation of the controller of Figure 4.9 giving the results of Figure 4.10.

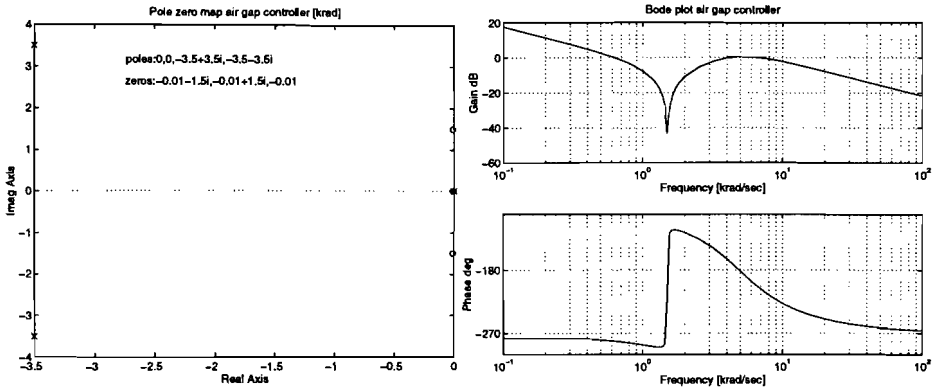

Figure 4.9 Pole zero map and bode plot of air gap controller.

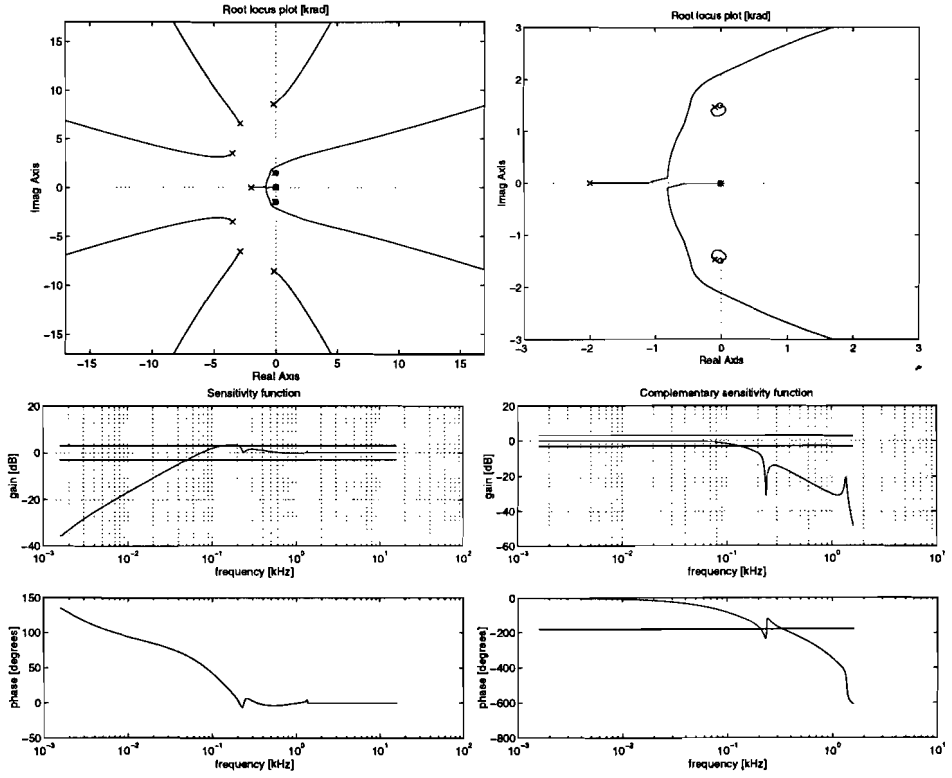

Figure 4.10 Closed loop transfer function of air gap control.

The sensitivity function has a -3-dB bandwidth of 50 Hz. The -3-dB bandwidth of the complementary sensitivity is about 100 Hz. As the control has a constant reference value the most 'honest'-value for bandwidth is the one given by the sensitivity function.

To test the disturbance suppression the PID controller is simulated with the following Simulink-blockscheme:

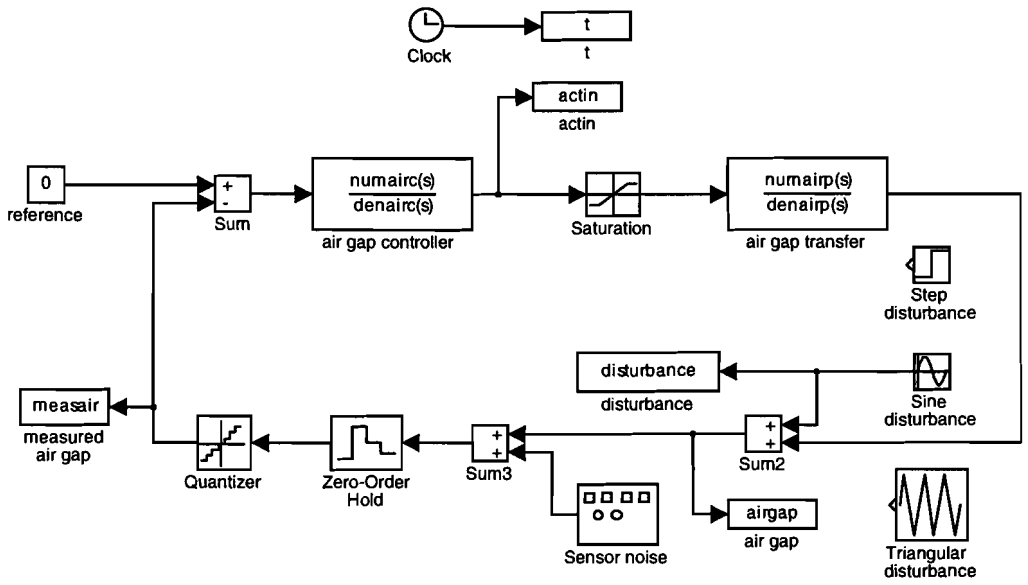

Figure 4.11 Simulink block scheme of the air gap control system.

The disturbances are added at the output of the process because in this way the measured disturbances can be used directly for simulations in simulink. The disturbances are caused by tilting of the mirror and by noise (relatively small). The disturbances caused by tilting the mirror can be modeled by either a ramp or sine function. The controller was tested also with a step as disturbance. Except from noise a step won't occur but it will give a good indication when actuator saturation can be expected. When the sine or ramp disturbance stays below the amplitude of the step when saturation occurs saturation will probably not occur.

The sensor resolution is simulated by noise with an maximum amplitude equal to 1 mV. The quantisation step is chosen equal to 20/2^16. The AD (Analog to Digital converter) input level should lay between +10 to -10 Volt and because the AD has a 80 dB SNR it has a effective resolution of 13 bits, but the quantisation is still done with 16 bits. The actuator saturation level was chosen equal to 0.5 Volts. (It could be some (25%) higher but this value wasn't a limitation for the controller used and in this way there is no risk for damage.)

Below the simulated responses to a step, sine and ramp disturbance are shown.

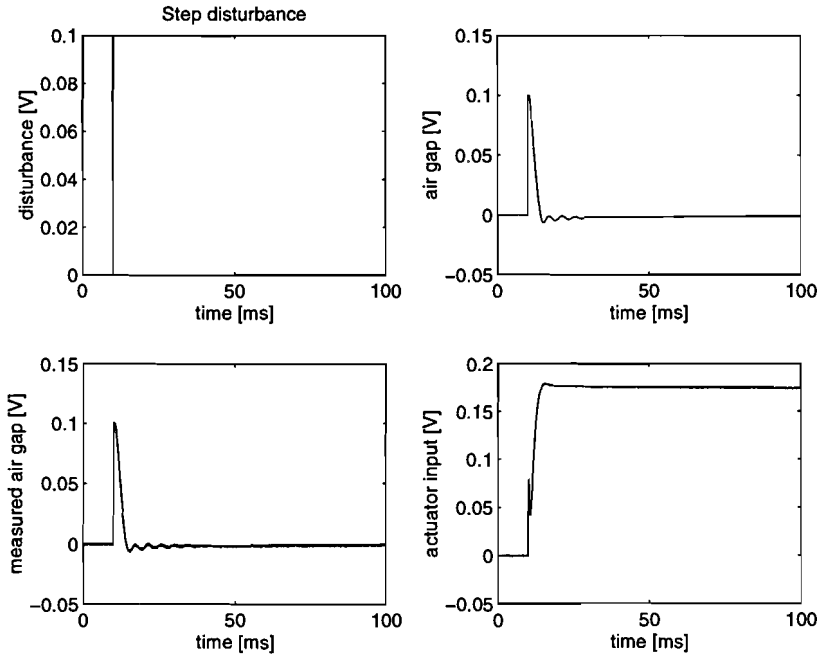

Figure 4.12 Simulated response to step disturbance.

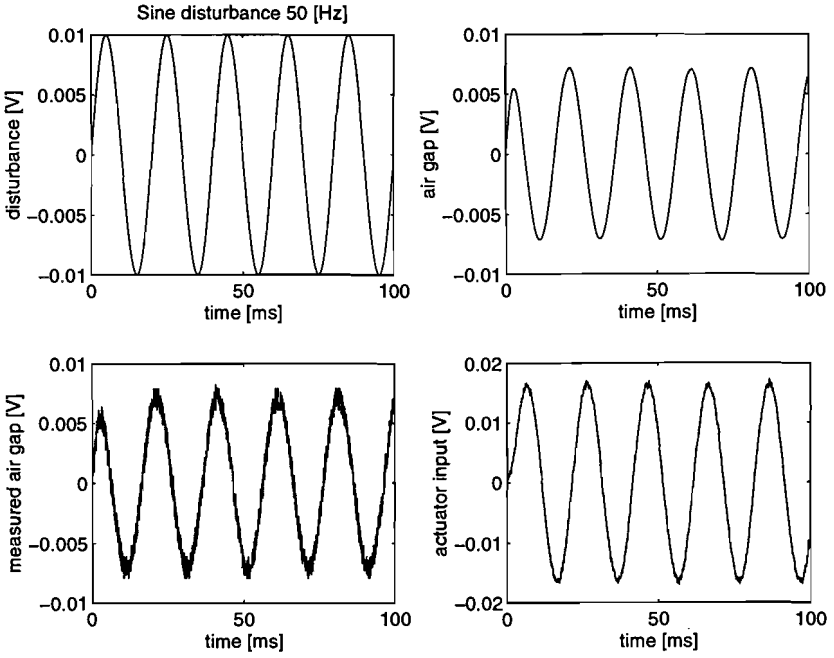

Figure 4.13 Simulated response to sine disturbance.

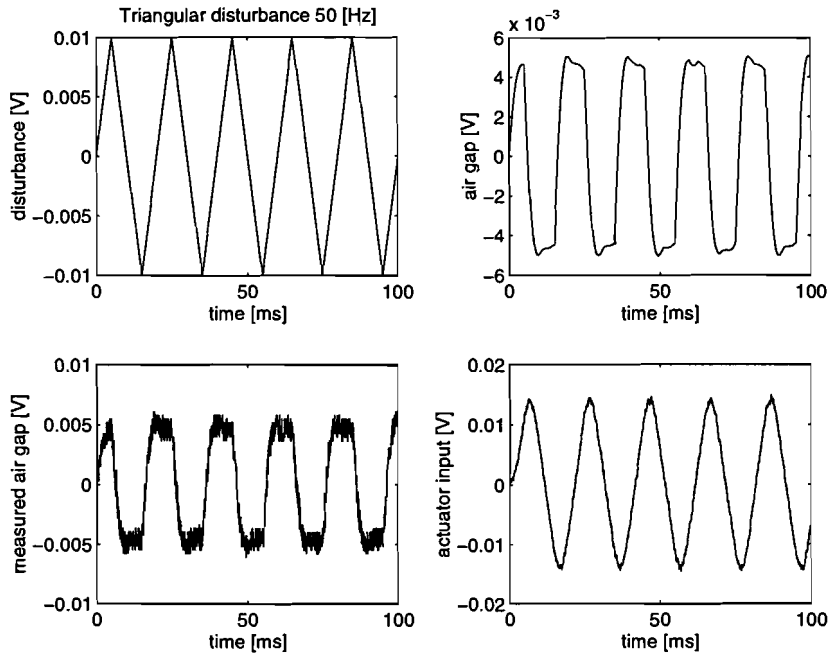

Figure 4.14 Simulated response to triangular disturbance.

The controller was implemented with the dSPACE system using the blockscheme of Figure 4.17.

The switches are added to start the controller with COCKPIT after compilation and turning on the remote control. (During compilation some signal changes occur on the outputs of the DA-convertor. To prevent arrival of these outputs to the actuators the remote control had to be switched of.)

To compare the simulation with the practical response disturbances were added with the dSPACE system (see Figure 4.17) and the simulated and practical air gap (sensor output [V]) were compared.

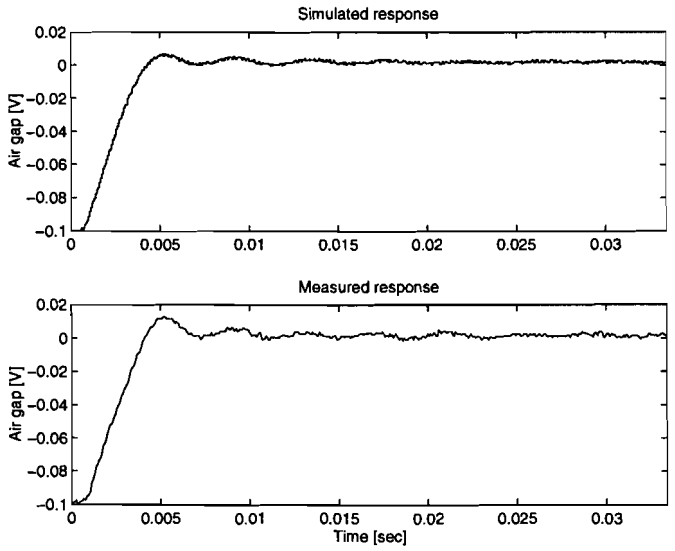

Figure 4.15 Simulated and practical step disturbance rejection.

The practical system shows some more overshoot. This means that the identified process has a smaller bandwidth. The noise in the practical system seems to be lower frequent. This is because the data is downsampled when saved.

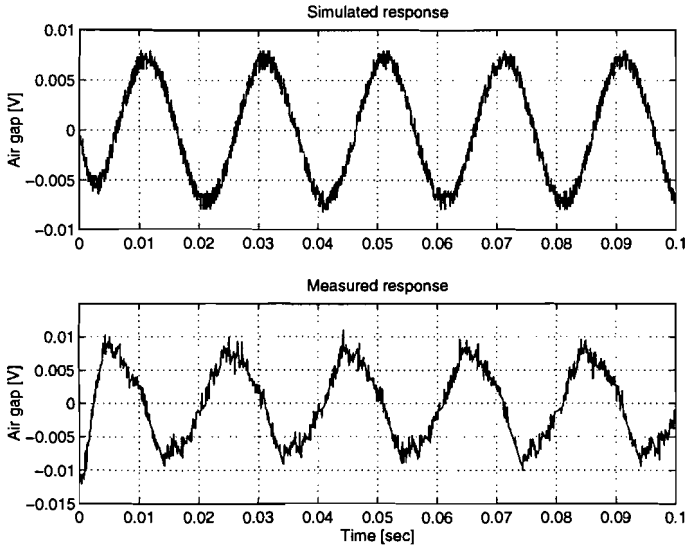

Figure 4.16 Simulated and practical sine disturbance rejection.

The picture shows a 3-dB attenuation of a 10 mV 50 Hz disturbance.
There are three differences: the practical response shows more but slower noise and there is a phase delay. The noise is slower because of the data acquisition. The practical system adds some more noise than the simulated system because the AD-convertor has a SNR of 80 dB which isn't simulated. The disturbances were added and started with the dSPACE system. The data acquisition should have started at the same time as the disturbance was started. However, there seems to be a delay between the two because the measured air gap doesn't start in 0 but has clearly a 'start-offset' (this has been several measurements). Why this happens with the sine disturbance and not with a step disturbance and only if data is saved with the automatic storage facility hasn't been solved yet. The practical sine disturbance shows similar distortion at the peaks, this is due to nonlinear effects. When analyzing the response with the spectrum analyzer there is not only a peak at 50 Hz but there are also peaks at 100 and 150 Hz (Peaks at higher frequencies get lost in noise.). For example the turning up of the mirror mentioned briefly in section 3.1.3.2 introduces nonlinearity.

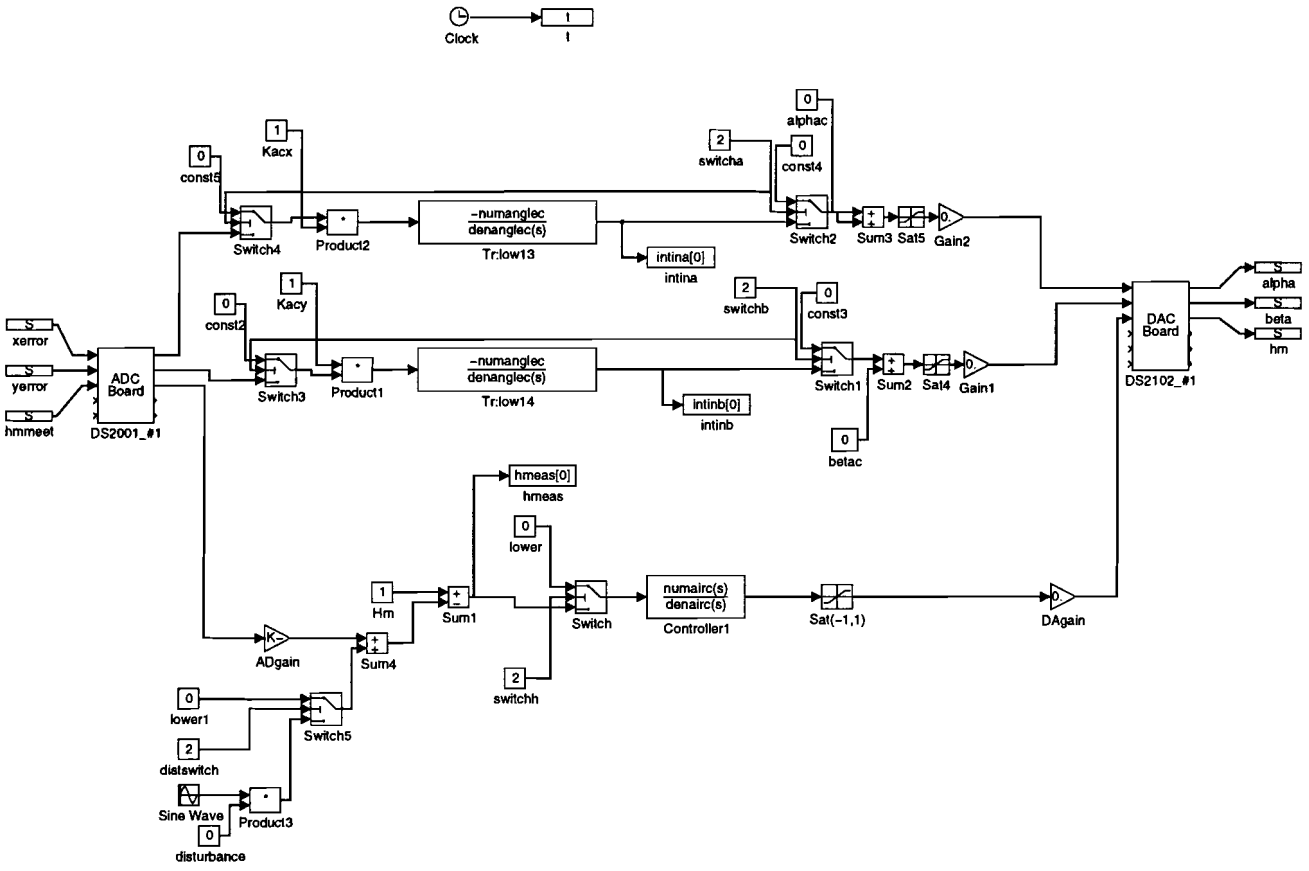

Figure 4.17 Block scheme used for implementation with dSPACE.

4.2 THE ANGLE CONTROLLER.

4.2.1 INTRODUCTION.

In Chapter 1 it became clear that the angle control loop for the tracking controller contains an optical path. Is it therefore necessary to make a model of the mirror plus the optical path and define this as the process to be controlled? If use is made of the control scheme below this isn't necessary.

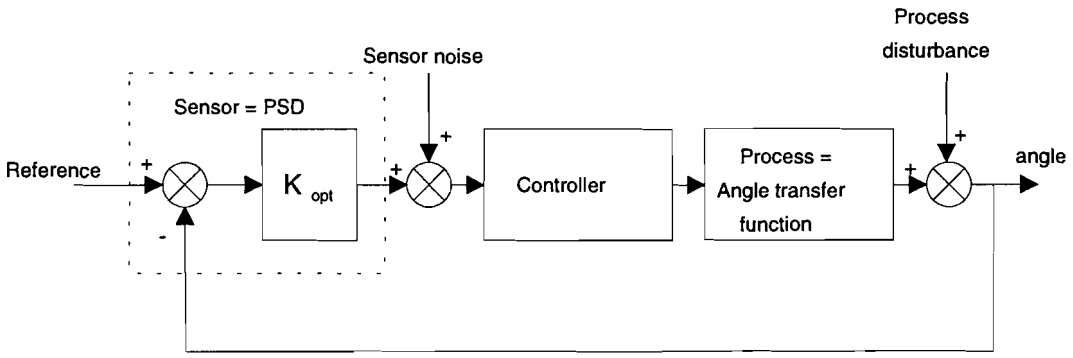

Figure 4.18 Control scheme for tracking mode (angle part).

The angle transfer function of the mirror is defined as process. The middle of the retroreflector defines the reference angle. A measure for the error between the reference and the angles of the mirror is obtained from the output of the PSD. The (partially) unknown factor is K_{opt}. 'Partially' is used because K_{opt} consists of the gain of the PSD which is known and the gain/attenuation of the optical path which varies between an upper and lower limit. In the different kinds of CD's (CD-ROM, CD-I, CD) the same control scheme is used.

Before implementing this scheme a closer look is taken at the angle transfer function.

4.2.2 TRANSFER FUNCTION ADJUSTMENT.

To determine the angle transfer function in the same way as was done for the air gap transfer function would be very hard. One would need to use the output of the secondary coils. As was explained in the previous chapter the outputs are only reliable if the air gap controller is able to hold the reference value. With the air gap controller designed in the previous section the angle transfer function measurement wouldn't reach a frequency high enough to use it for building an angle controller. However, it is possible to verify the positions of the poles (angle transfer function contains no zeros) of the theoretical model.

The model, see Chapter 2 page 6, predicts three poles: -3757, -226 and at -17. If an integrator in the origin is used as controller, the root locus plot will show that the poles at 0 and -17 combine and break away causing a crossing of the jw-axis. So if we implement this controller and choose as starting point a low gain (e.g. the gain at the break away point), the gain can then be tuned up till the tracking starts oscillating. The actual gain can be determined by

comparing the gain set with the gain predicted by the root locus and the measured oscillating frequency allows the calculation of the actual position of the pole. By choosing other pole zero combination the other poles can also be checked. This procedure should be done several times because after adjusting the other poles of the system the break away point will change and therefore the crossing with the jw-axis will also change.

The actual pole positions were found to be -60,-140,-1775. This last pole is introduced by the transfer from the force on the actuators to the voltage applied to them and determined by the impedance parameters of the actuator coil, and is therefore also present in the air gap transfer function. The measurement of the air gap transfer showed a pole at -1998. The discrepancy can be explained by measurement errors, the difference between the identification and the true process and the identification of the air gap transfer function gave two extra poles. These will also translate the pole at -1998.

The transfer function obtained in this way was used for controller design.

4.2.3 CONTROLLER DESIGN AND IMPLEMENTATION.

The controller should have a zero-steady state error for steps. This means that the control should contain at least one pole in the origin. As was extensively discussed in one of the previous sections, the air gap transfer function contains resonance frequencies around the 350 Hz. Because the angle transfer couldn't be measured we don't have an answer to the question: "Contains the angle transfer function the same resonance frequencies?". During testing of different controllers and the determination of the poles as discussed in the previous section it was noticed that the system had the tendency to oscillate with 340 Hz. Together with the fact that the underlying system is the same for the angle and air gap one can draw the conclusion that the angle transfer functions contains also resonance frequencies around 350 Hz. The Q-factor of these resonance frequencies are unknown. Therefore the controller should have attenuation around 350 to suppress the three resonance frequencies. The practical implementation of the controller shows when the attenuation is enough.

The following controller was tested on the real system:

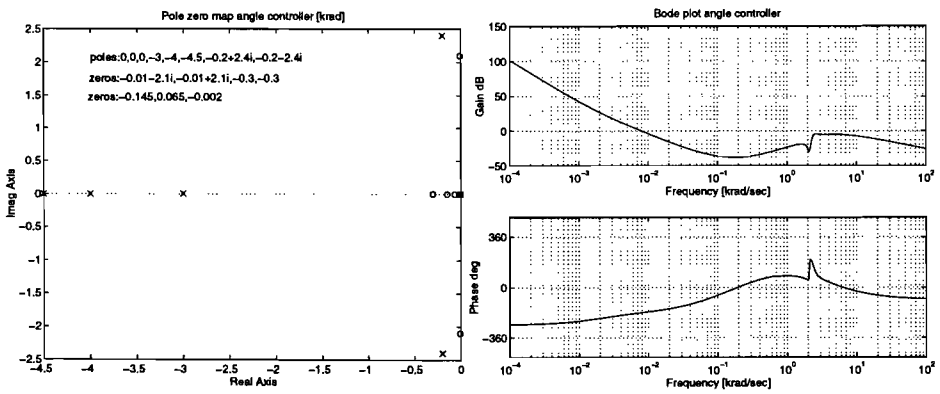

Figure 4.19 Pole zero map and bode plot of angle controller.

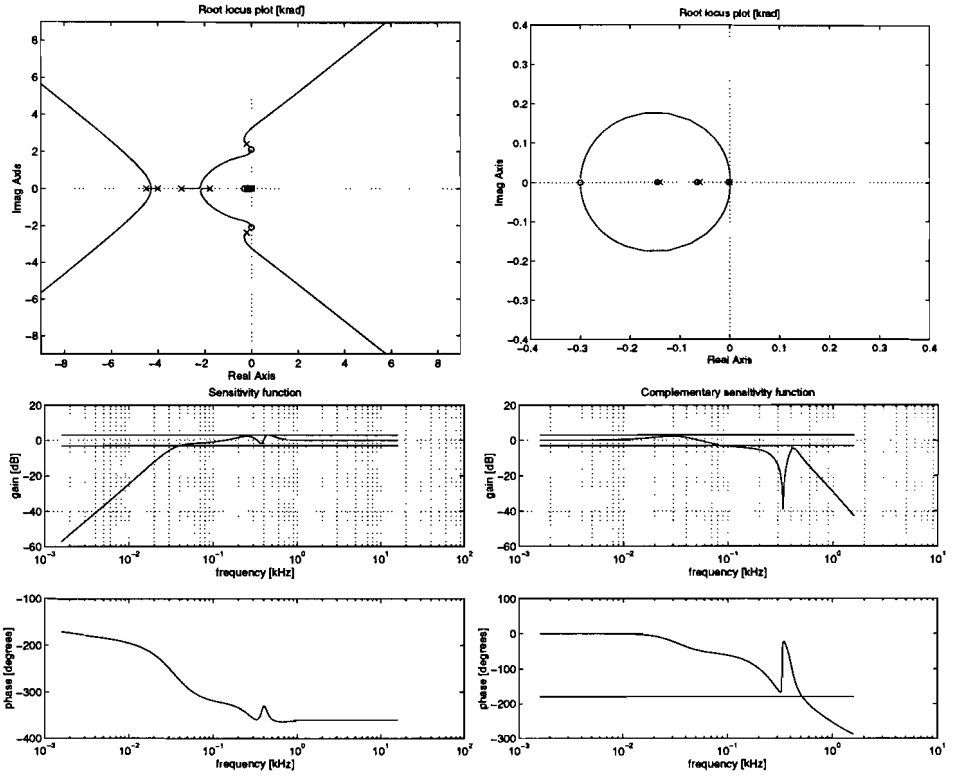

Figure 4.20 Closed loop transfer function of angle controller.

A pole-zero combination is placed around 350 Hz to provide attenuation. Whether the placement is correct can only be tested in practice. Because it is possible that the root locus will show a different kind of behavior and makes the system unstable for a lower gain than calculated.

The PID controller is simulated with the following Simulink-blockscheme:

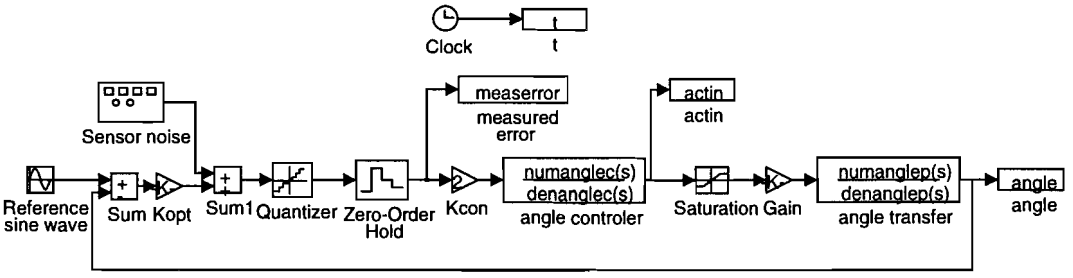

Figure 4.21 Block scheme of the angle control system.

Only one angle is simulated because in the linearized model the angles α and β aren't coupled.

The sensor resolution is simulated by noise with an maximum amplitude equal to 1 mV. The quantisation step is chosen equal to 20/2^16.

The maximum value that can be applied to the actuators is determined by mechanical constraints. Because a higher excitation frequency is attenuated more by the process then a low excitation frequency, the value at which the mirror will hit its bearing, the actuator

saturation value, will increase with frequency. However it isn't possible to translate a maximum value in the frequency domain to a maximum value in the time domain. Therefore we have to be satisfied by using the lowest actuator saturation value. This is obtained at f=0 Hz.

To determine this value, the amplitude of a DC-signal on the α-angle control input was increased till the semi sphere touched the bearing in which it is floating. In practice (control loop running) this has to be prevented so the actuator saturation value was chosen equal to 0.2 Volt about 10% smaller than the determined value.

To compare simulation results with practical results isn't done as easy as with the air gap controller.
- There is no optical filter placed in front of the PSD. This gives distortion of which the influence depends on the brightness of the daylight (During testing all the TL were switch of to cancel out this disturbance.) and in relation to the power of the laser used. In the ideal situation one would have 0 V if there is no laser on the PSD and ±10 V if the laser points at the outside of the PSD.
- The angle sensors aren't calibrated. Therefore it isn't possible to measure the angle's of the mirror exactly.

In the test setup the retroreflector was attached to a wheel on the shaft of a motor. The radius of the circle the retroreflector makes is about 11 cm. This means that we have a sine-excitation in x and y direction around an offset facilitating the comparison of simulation with practical results.

With this setup the second problem can be solved. If we subtract the mean value of the actuator inputs (collected during a certain interval) from each sample an approximation is obtained of the situation when the retroreflector would make turns without offset. With the amplitude of the actuator input the angle can be calculated because the maximum value 0.2 is equal to ±23 degrees. And the process that transforms the actuator input to an angle is known. This method makes a comparison of the error obtained from the simulation with the errors collected during an experiment possible.

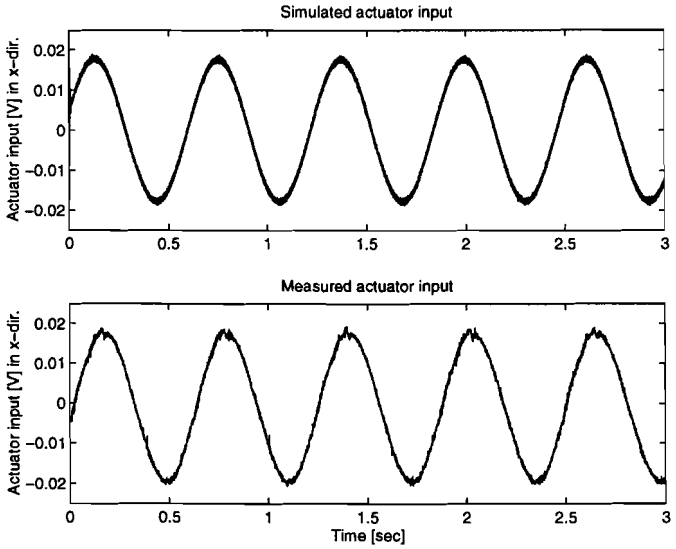

Figure 4.22 Simulated and practical actuator input.

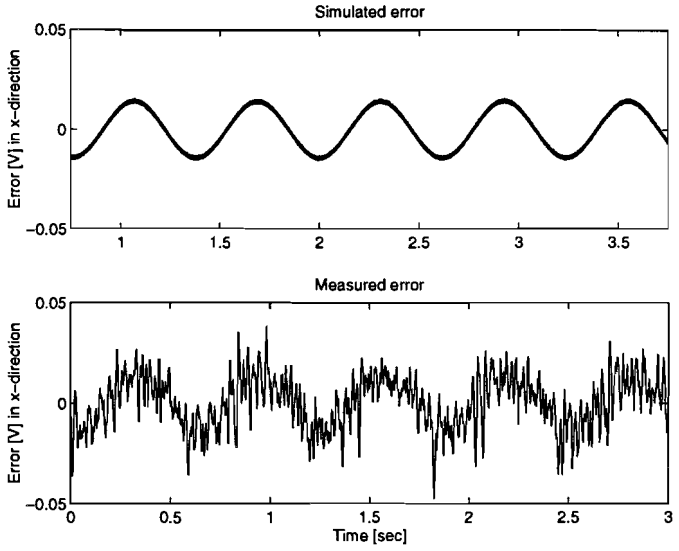

Figure 4.23 Simulated and practical error in x-direction.

Both simulations have a phase delay in relation to the practical response because the measurement is started random during a rotation of the retroreflector and the simulation starts with a sine having a phase of 0 degrees.

The actuator inputs have a slight amplitude difference caused by the way in which the reference value is calculated and because of the fact that the gain of the identified and practical transfer function will differ. The noise in the simulated response is denser because a downsampling factor of 10 is used (This was necessary to prevent a buffer overflow.).

The (mean) amplitude and frequency of the error simulation and measurement are the same. With this amplitude the laser spot is positioned at about 2/3 of the 'radius' of the PSD. However, there is a large difference between the instantaneous values. The 'slow' difference is due to the turning of the retroreflector. In the simulations a sine is chosen as reference but in practice this is a noisy sine because the shaft to which the gear is connected is oval and the motor with servo amplifier has trouble turning around the weight of the retroreflector. The fast variations are caused by the laser spot that hits the PSD. This spot isn't symmetrical. As the retroreflector turns, the PSD sees not only a dot that has an offset, because the tracking isn't able to follow, but also the spot has turned. This will influence the calculation of the center of the spot. From the response of the PSD a spectrum plot was made. Figure 4.24 shows clearly higher harmonics of 1.6 Hz. These are caused by:
1. The retroreflector only approximates a sine. In the simulation a sine was taken as excitation for simplicity.
2. The process will be nonlinear.

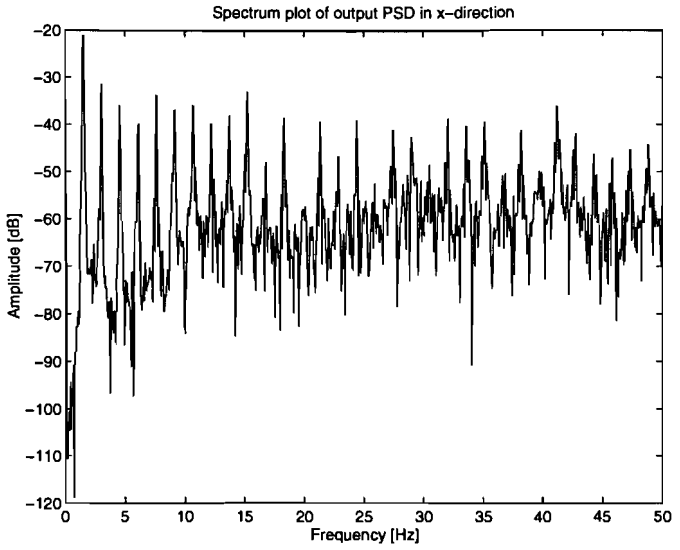

Figure 4.24 Spectrum plot of output PSD in x-direction.

5. CONCLUSIONS AND RECOMMENDATIONS.

5.1 SENSORS.

Conclusions angle sensor:

- Measurements showed that the primary coil had a very low $\omega L/R_L$ (1.58 at 40 kHz the frequency used in the old setup). In spite of the fact that the new electronics limits the frequency to 20 kHz, $\omega L/R_L$ was increased to 5.4 (at 18 kHz). The increase of this quality factor was realized by increasing the cross sectional copper area of the primary coil.
- For the angle measurement new sensor electronics were developed. The sensors (two secondary coils) are based on two LVDT-signal conditioners of which one is used as master (driving the primary coil) and the other as slave. This IC divides the measured voltage over the secondary coil by the voltage measured over the primary coil. This means that amplitude drift of the voltage supplied to the primary coil is annihilated.
- The voltage measured over the primary coil consists of two 'parts'. The voltage over the inductance and the voltage over the resistance. If the temperature changes R_L changes. This means that the voltage over the inductance changes causing an amplitude change at the secondary side. The LVDT doesn't see this change at the primary side. Because the new primary coil is still of low quality this change has a large influence on the measurement. Therefore a circuit was added to the LVDT-IC that subtracts the voltage over R_L at 27^o (or the mean temperature at which the circuit is going to be used) from the voltage over the primary coil. In this way the influence of R_L becomes about 20 times smaller.

Conclusions air gap sensor:

- For the air gap sensor two electronic processors were build. One sensor was based on the old principle and the other on the LVDT-signal conditioner used as slave. The great advantage of the later one is again the annihilation of amplitude drift. The former one can be used if the air gap sensor has to be driven with a higher frequency.

Conclusions crosstalk:

- The angle measurement influences the air gap sensor. A quantitative measurement of this influence as function of the tilting of the mirror hasn't been determined. If it turns out that this influence is too big and can't be solved by lowering the parasitic capacitances one needs to use other frequencies for both measurements.

Recommendation:

- Measurements should be done to quantify the influence of the tilting of the mirror on the air gap measurement and vice versa because the same carrier frequency is used for both measurements.

5.2 AIR GAP CONTROL.

Conclusions:

- Using the servo mode of the SA the measurement of the air gap transfer function makes a measurement of the transfer function possible with a coherence greater than 0.95. The measurement revealed resonances at 350 Hz. Besides these resonances there are several resonances of which the frequencies depend on the air gap.
- An PID controller has been developed having a bandwidth of 50 Hz.

Recommendations:

- Further research should be done to reveal the origin of the resonance frequencies at 350 Hz. If it would be possible to remove them a higher bandwidth would be possible.
- Because we are dealing with a transfer function depending on the air gap this process is an ideal candidate for H∞-control or μ analysis/synthesis.

5.3 ANGLE CONTROL.

Conclusions:

- The implementation of well chosen controllers makes it possible to adjust the poles from the theoretical model to the poles as they are in practice. The adjusted theoretical transfer function was the basis of the PID-controller developed.
- The angle transfer function contains also the resonances frequencies at 350 Hz, revealed by the measurement of the air gap transfer function.

Recommendations:

- An optical bandpass filter (the laser belonging) should be placed in front of the PSD.
- Also here we are dealing with a process of which the position of the poles are only known to a certain extent. H∞-control or μ analysis/synthesis should be worth studying for robustness sake.

Appendix A

For the values of $\underline{F}(t)$, $G(\underline{p})$ and $g(\underline{p})$ see [Noten]. In this appendix only $Q(\underline{v},\underline{p},t)$ and $M(\underline{p})$ are repeated because they contain an error in [Noten].

$$M = \begin{pmatrix} j_{xy} & 0 & 0 & \\ 0 & j_{xy} & 0 & 0 \\ 0 & 0 & j_z & \\ & 0 & & mI \end{pmatrix}$$

j should be taken different values as there is an inertia in the xy-plane and the z-plane.

$$\underline{Q} = \begin{pmatrix} -\left\{\dfrac{1+\xi^2}{(1+T_\alpha^2)C_\beta}k_1 - j\dfrac{S_{2\alpha}T_\beta(\xi\dot{\beta}+\dot{\phi}'\sqrt{1+\xi^2})((C_\beta+T_\alpha\xi)\dot{\alpha}-T_\alpha S_\beta\dot{\beta})}{1+\xi^2}\right\} \\ -\left\{-j\dfrac{(\xi\dot{\beta}+\dot{\phi}'\sqrt{1+\xi^2})((C_\beta+T_\alpha\xi)\dot{\alpha}-T_\alpha S_\beta\dot{\beta})}{1+\xi^2}\right\} \\ -\left\{-j\dfrac{(\dot{\beta}\sqrt{1+\xi^2}+\xi\dot{\phi}')((C_\beta+T_\alpha\xi)\dot{\alpha}-T_\alpha S_\beta\dot{\beta})}{1+\xi^2}\right\} \\ -D\dot{h}_1 - Kh_1 \\ -D\dot{h}_2 - Kh_2 \\ -D\dot{h}_3 - Kh_3 \end{pmatrix}$$

Appendix B

$a=L(2j+3r^2m)$
$b=3r^2DL+3r^2mR+2jR$
$c=3r^2(DR+KL+A^2)$
$d=3r^2KR$

Parameter	Value	Description
A	3.16 [$kg \cdot m \cdot s^{-2} \cdot A^{-1}$]	Actuator constant depending on coil radius, number of windings and magnitude of the magnetic field
D	0 [$N \cdot s \cdot m^{-1}$]	Damping
j	$10.6 \cdot 10^{-8}$ [$kg \cdot m^2$]	Moment of inertia around the centre of the mirror's surface, in xy-plane
L	10^{-3} [H]	Induction of the coil
m	$9.5 \cdot 10^{-3}$ [kg]	Mass of coil
r	$7.0 \cdot 10^{-3}$ [m]	Distance from center of mirror to connection of actuator string.
R	4 [Ω]	Resistance of the coil

Appendix C

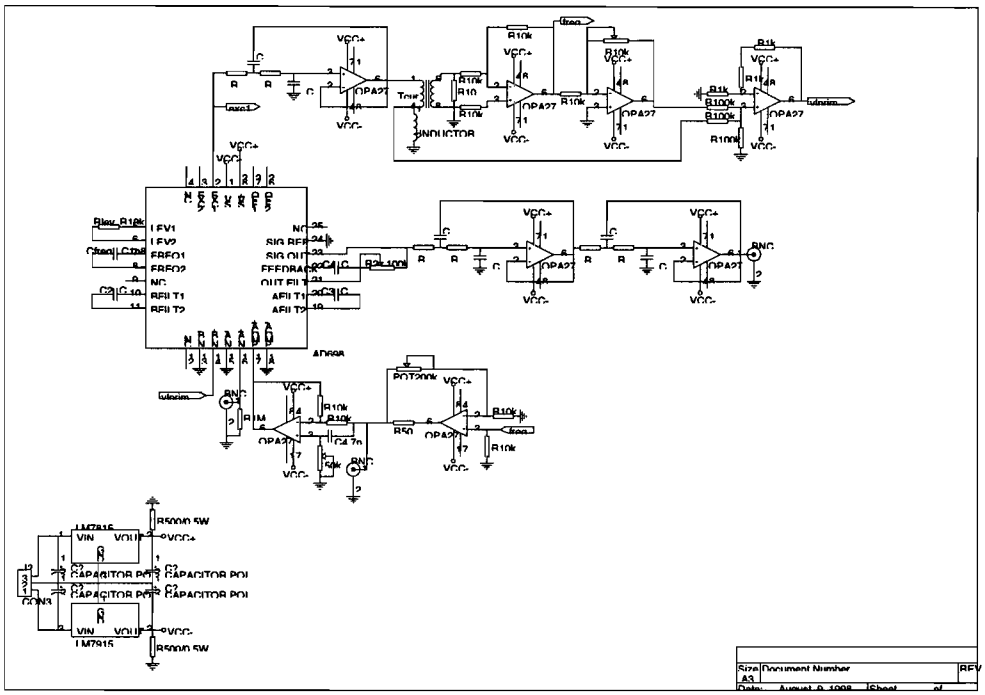

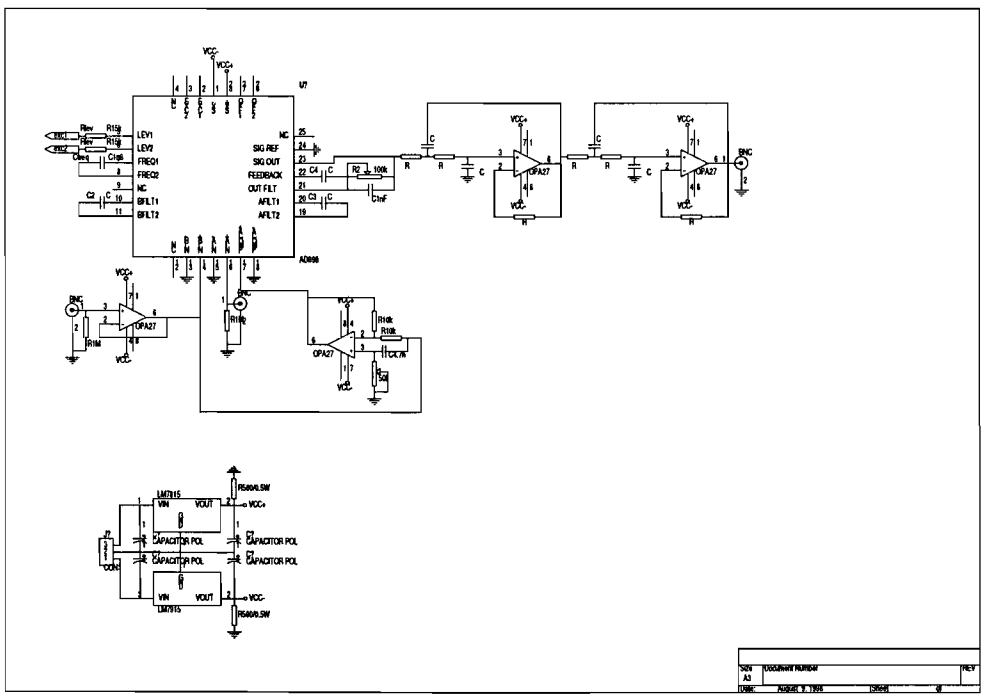

Bibliography

H.J. Goossens. Modeling and simulation of a laser deflecting system. Final thesis report, Eindhoven: University of Technology, 1995.

A. F. Kip. Elektriciteit en magnetisme. Prisma-Technica 6. Uitgeverij het spectrum N.V. , 1970.

R.L.M. Looymans. H∞-control of the air gap of a laser deflecting system. Final thesis report, Eindhoven: University of Technology, 1997.

M.A. Noten. Controlling of a laser deflecting system. Final thesis report, Eindhoven: University of Technology, 1997.

F.Sass, Ch.Bouche, A.Leitner. Duebbels Taschenbuch fuer den Maschinenbau. Springer-Verlag, 1966

R.A. Zorge. Measurements on a miniature spherical air bearing by using its electrical capacitance. Measurement 11 (1993) 159-172. Elsevier, 1993.

R.A. Zorge. Sheets ER-seminaria 23 september 1997.